ASTROBIOLOGY
Volume 16, Number 11, 2016
Mary Ann Liebert, Inc.
DOI: 10.1089/ast.2015.1422

# The Pale Orange Dot: The Spectrum and Habitability of Hazy Archean Earth

Giada Arney,[1,2,3,4,5] Shawn D. Domagal-Goldman,[2,6] Victoria S. Meadows,[1,2,3]
Eric T. Wolf,[7] Edward Schwieterman,[1,2,3,5,8,9] Benjamin Charnay,[1,2,3,10]
Mark Claire,[2,9,11] Eric Hébrard,[6,12] and Melissa G. Trainer[6]

## Abstract

Recognizing whether a planet can support life is a primary goal of future exoplanet spectral characterization missions, but past research on habitability assessment has largely ignored the vastly different conditions that have existed in our planet's long habitable history. This study presents simulations of a habitable yet dramatically different phase of Earth's history, when the atmosphere contained a Titan-like, organic-rich haze. Prior work has claimed a haze-rich Archean Earth (3.8–2.5 billion years ago) would be frozen due to the haze's cooling effects. However, no previous studies have self-consistently taken into account climate, photochemistry, and fractal hazes. Here, we demonstrate using coupled climate-photochemical-microphysical simulations that hazes can cool the planet's surface by about 20 K, but habitable conditions with liquid surface water could be maintained with a relatively thick haze layer ($\tau \sim 5$ at 200 nm) even with the fainter young Sun. We find that optically thicker hazes are self-limiting due to their self-shielding properties, preventing catastrophic cooling of the planet. Hazes may even enhance planetary habitability through UV shielding, reducing surface UV flux by about 97% compared to a haze-free planet and potentially allowing survival of land-based organisms 2.7–2.6 billion years ago. The broad UV absorption signature produced by this haze may be visible across interstellar distances, allowing characterization of similar hazy exoplanets. The haze in Archean Earth's atmosphere was strongly dependent on biologically produced methane, and we propose that hydrocarbon haze may be a novel type of spectral biosignature on planets with substantial levels of $CO_2$. Hazy Archean Earth is the most alien world for which we have geochemical constraints on environmental conditions, providing a useful analogue for similar habitable, anoxic exoplanets. Key Words: Haze—Archean Earth—Exoplanets—Spectra—Biosignatures—Planetary habitability. Astrobiology 16, 873–899.

---

[1] Astronomy Department, University of Washington, Seattle, Washington, USA.
[2] NASA Astrobiology Institute Virtual Planetary Laboratory, University of Washington, Seattle, Washington, USA.
[3] Astrobiology Program, University of Washington, Seattle, Washington, USA.
[4] Now at: NASA Goddard Space Flight Center, Greenbelt, Maryland, USA.
[5] Now at: NASA Postdoctoral Program, Universities Space Research Association, Columbia, Maryland, USA.
[6] NASA Goddard Space Flight Center, Greenbelt, Maryland, USA.
[7] Department of Atmospheric and Oceanic Sciences, Laboratory for Atmospheric and Space Physics, University of Colorado at Boulder, Boulder, Colorado, USA.
[8] Now at: University of California at Riverside, Riverside, California, USA.
[9] Blue Marble Institute of Science, Seattle, Washington, USA.
[10] Now at: Paris-Meudon Observatory, Paris, France.
[11] Department of Earth and Environmental Sciences, University of St Andrews, St Andrews, UK.
[12] University of Exeter, Exeter, Devon, UK.

## 1. Introduction

Early in Earth's history, an anoxic atmosphere could have supported the formation of an organic haze (Pavlov *et al.*, 2001a; Trainer *et al.*, 2004, 2006; DeWitt *et al.*, 2009; Hasenkopf *et al.*, 2010; Zerkle *et al.*, 2012; Kurzweil *et al.*, 2013; Claire *et al.*, 2014; Izon *et al.*, 2015) that strongly interacted with visible and UV radiation, cooling the planet's climate (Pavlov *et al.*, 2001b; Domagal-Goldman *et al.*, 2008; Haqq-Misra *et al.*, 2008; Wolf and Toon, 2010; Hasenkopf *et al.*, 2011). This hydrocarbon haze, generated by methane ($CH_4$) photolysis, would have formed when the ratio of $CH_4$ to carbon dioxide ($CO_2$) in the atmosphere exceeded about 0.1 (Trainer *et al.*, 2006).

Unlike the hazes that may exist around exoplanets with thick hydrogen-dominated atmospheres (Sing *et al.*, 2011; Knutson *et al.*, 2014; Kreidberg *et al.*, 2014), the Archean (3.8–2.5 billion years ago) haze was likely biologically mediated via $CH_4$ produced from methanogenesis, one of the earliest metabolisms (Woese and Fox, 1977; Ueno *et al.*, 2006). In addition, several abiotic processes including serpentinization (the hydration of ultramafic rocks, mainly olivine and pyroxenes) can form methane (Kelley *et al.*, 2005; Etiope and Sherwood Lollar, 2013; Guzmán-Marmolejo *et al.*, 2013), but the biotic flux of methane to the Archean atmosphere was likely much higher than the abiotic flux (Kharecha *et al.*, 2005), as it is on Earth today. While the climatic effects of this haze have been studied (*e.g.*, Pavlov *et al.*, 2001b), impacts of haze on Archean Earth's habitability have not been previously investigated using tightly coupled climate-photochemical models. This coupling is critical to consider because of potential feedbacks between the impact of temperature on haze formation and the effects of haze on the atmosphere's temperature structure. Additionally, although we anticipate planetary diversity in the exoplanet population, existing spectral studies are largely focused on the observables of modern-day Earth (*e.g.*, Sagan *et al.*, 1993; Woolf *et al.*, 2002; Robinson *et al.*, 2011, 2014a). Those spectral studies that consider Archean Earth and anoxic planets have not examined hazes (Meadows, 2006; Kaltenegger *et al.*, 2007; Domagal-Goldman *et al.*, 2011). As we will show, hydrocarbon haze has profound spectral impacts for both reflected light and transit transmission spectra.

### 1.1. Evidence for an Archean haze

Geochemical data suggest 3–5 distinct intervals of organic haze during the later Archean (Zerkle *et al.*, 2012; Izon *et al.*, 2015), supporting theoretical studies on the causes and consequences of photochemical haze formation in the atmosphere (Pavlov *et al.*, 2001a, 2001b; Domagal-Goldman *et al.*, 2008; Haqq-Misra *et al.*, 2008; Kurzweil *et al.*, 2013; Claire *et al.*, 2014) as well as experimental data (Trainer *et al.*, 2004, 2006; DeWitt *et al.*, 2009; Hasenkopf *et al.*, 2010, 2011) and theory on their potential radiative effects (Wolf and Toon, 2010). The geochemical evidence, described below, implies Neoarchean hazy intervals (Zerkle *et al.*, 2012; Izon *et al.*, 2015) lasting for less than 1 million years. The constraint on the duration of these intervals is based on the lower limit of shale sedimentation rates. In addition, the modeling work of Domagal-Goldman *et al.* (2008) suggests a longer Mesoarchean to Neoarchean hazy period between 3.2 and 2.7 Ga.

Here, we present an overview of the evidence for the Archean haze. The line of evidence most often invoked comes from analyses and modeling of sulfur isotope fractionation data from Earth's rock record. Several studies have proposed links between haze and the mass-independent sulfur isotope fractionation signal (S-MIF) (Farquhar *et al.*, 2000) preserved in the geological record before the Great Oxygenation Event (GOE) at about 2.5 Ga (Domagal-Goldman *et al.*, 2008; Zerkle *et al.*, 2012; Kurzweil *et al.*, 2013; Claire *et al.*, 2014; Izon *et al.*, 2015). We present a brief review of this evidence here, beginning with an overview of sulfur mass-independent fractionation, on which much of the evidence for an Archean haze is based.

Sulfur has four stable isotopes: $^{32}S$, $^{33}S$, $^{34}S$, and $^{36}S$. Isotope fractionations are reported in parts per thousand (‰) using delta notation ($\delta$) such that

$$\delta^x S = \left[\frac{^xR_{\text{sample}}}{^xR_{\text{standard}}} - 1\right] \times 10^3 \ [‰] \qquad (1)$$

Here, $^xR_{\text{sample}}$ represents isotope ratios of the given minor to major isotope (for sulfur, $^xR$ means $^xS/^{32}S$ with $x = 33, 34, 36$) of sampled material. $^xR_{\text{standard}}$ represents isotope ratios of a standard reference material.

Reactions following classical equilibrium or kinetic behaviors produce isotope fractionation that depend only on the mass differences of the isotopes such that the $\delta^{33}S$ composition of a material is approximately half the $\delta^{34}S$ amount, and the $\delta^{36}S$ composition is roughly twice the $\delta^{34}S$ amount. For elements with more than two stable isotopes, mass-dependent fractionation (MDF) quantifies this expected three-isotope relationship, and samples following MDF will have $\delta^{33}S \sim 0.515 \times \delta^{34}S$ and $\delta^{36}S \sim 1.89 \times \delta^{36}S$.

Mass-independent fractionation (MIF) occurs when samples deviate from this expected three-isotope behavior and is quantified with "capital delta" notation where $\Delta^{33}S = \delta^{33}S - 0.515 \times \delta^{34}S$ and $\Delta^{36}S = \delta^{36}S - 1.89 \times \delta^{36}S$. MIF in naturally occurring samples is very unusual and is generally diagnostic of quantum chemistry such as can occur in certain atmospheric reactions. While the precise mechanism (or mechanisms) that produces S-MIF is unknown, photolysis of sulfur gases in an anoxic atmosphere is the only known mechanism that produces large-magnitude $\Delta^{33}S$ and $\Delta^{36}S$ seen in the rock record (Farquhar *et al.*, 2001, 2007).

The S-MIF signal is variable throughout the Archean, and it vanishes completely once $O_2$ builds up to non-negligible levels in the atmosphere after the GOE at 2.5 Ga. Its recurrence at both ends of the Archean eon implies that, within 0.8 billion years of Earth's formation, a common mechanism for S-MIF production was already established in the atmosphere (Thomassot *et al.*, 2015). After the GOE, $O_2$ and the ozone ($O_3$) derived from $O_2$ photochemical reactions block the UV photons necessary to photolyze sulfur gases and produce S-MIF. Also, $S_8$ is the most important species to rain out S-MIF from the atmosphere; because a more reducing atmosphere enhances the ability of $S_8$ to polymerize, S-MIF is more easily preserved under reducing conditions (Zahnle *et al.*, 2006). After the GOE, all the sulfur in the atmosphere would have been oxidized into a single exit channel, eliminating any fractionation created in the atmosphere (Pavlov and Kasting, 2002). Thus, S-MIF is generally regarded as robust evidence for an anoxic Archean atmosphere.

$\Delta^{33}S$ typically correlates with enrichments in $\delta^{34}S$ and with depletions in $\delta^{36}S$, and variations in magnitude and sign of these isotopic signals in Earth's geological record hint that strong constraints on Archean atmospheric chemistry will be possible when the precise MIF formation mechanisms are identified (Claire *et al.*, 2014). $\Delta^{36}S/\Delta^{33}S$ in Archean sedimentary rocks is generally around −1, but stratigraphic variations in this slope have been observed in the geological record and interpreted as evidence of changes to the S-MIF production mechanism resulting from changes in atmospheric composition (Zerkle *et al.*, 2012; Kurzweil *et al.*, 2013; Izon *et al.*, 2015), suggesting the influence of haze.

Domagal-Goldman *et al.* (2008) and Haqq-Misra *et al.* (2008) studied potential links between S-MIF, hazes, and Archean glaciation. At ~2.9 Ga, there is geological evidence suggesting a glaciation event (Young *et al.*, 1998) may have occurred during the same period when the S-MIF $\Delta^{33}S$ signal dips to lower values. An upper atmosphere haze that decreased tropospheric $SO_2$ photolysis by blocking UV photons and cooled the planet could explain both the glaciation and the decrease in S-MIF. In this conceptual model, the end of the cold period typified by low $\Delta^{33}S$ may be due to a decrease in the atmospheric $CH_4/CO_2$ ratio, which would have cleared any haze present in the atmosphere. If true, this change in atmospheric composition and radiative scattering would have enabled UV photons to penetrate deeper into the atmosphere, interacting with sulfurous gases and affecting their isotopic signatures (Claire *et al.*, 2014). Earth's record of sedimentary sulfates does show a significant change in their minor sulfate isotope behavior between 2.73 and 2.71 Ga (Kurzweil *et al.*, 2013; Izon *et al.*, 2015) that may in fact reflect this change, although predictive models of sulfur isotope fractionation are not yet able to reproduce these trends seen in the rock record (Claire *et al.*, 2014).

Zerkle *et al.* (2012) discussed the discovery of geochemical evidence consistent with the Archean haze hypothesis. The authors analyzed sediments aged 2.65–2.5 Ga collected from the Ghaap Group in South Africa and showed that variations of $\Delta^{36}S/\Delta^{33}S$ associated with changes in atmospheric chemistry were contemporaneous with highly negative excursions of $\delta^{13}C_{org}$ values. Negative values of $\delta^{13}C_{org}$ below −37‰ are typically interpreted as evidence for methanogenesis (biological methane production) followed by subsequent incorporation into sediments by methanotrophy (methane consumption), which imparts a strongly negative $\delta^{13}C_{org}$ because organisms preferentially uptake the $^{12}C$ (Urey and Greiff, 1935; Schopf, 1983; Schidlowski, 2001; Eigenbrode and Freeman, 2006). The contemporaneous excursions of the sulfur and $C_{org}$ isotopes suggest a close linkage between S-MIF signals and biogenic methane. The links between S-MIF signals and biogenic methane production have been recently expanded over multiple cores and locations, suggesting multiple changes in atmospheric chemistry during the Neoarchean (Izon *et al.*, 2015). Changes observed in the slope of $\Delta^{36}S/\Delta^{33}S$ vary between −1.5 and −0.9 and are interpreted to reflect changes in the S-MIF source reactions driven by varying atmospheric haze thicknesses.

Kurzweil *et al.* (2013) noted that an increase in magnitude of S-MIF signals after 2.73 Ga (Thomazo *et al.*, 2009) occurred during a prolonged negative shift in $\delta^{13}C_{org}$, suggesting enhanced biological methane activity at this time. Similar to Zerkle *et al.* (2012), they discuss a change in the slope of $\Delta^{36}S/\Delta^{33}S$ from −1.5 to −0.9 at 2.71 Ga and interpret this to be caused by a decrease in the $CH_4/CO_2$ ratio at 2.71 Ga, possibly indicating an organic haze was present for some period of time prior to 2.71 Ga and cleared afterward. In this interpretation, haze-free and reducing atmospheric conditions dominated after 2.71 Ga, with haze reappearing in brief intervals of time as suggested by the Zerkle *et al.* (2012) and Izon *et al.* (2015) measurements.

Given the apparent occurrence of haze in the Archean, we investigated the impact of this haze on the climate, spectral appearance, and surface UV flux by simulating the hazy Archean environment with boundary conditions consistent with recent geochemical constraints. Unlike previous studies of the Archean climate under a haze, we use realistic fractal (rather than spherical) particles, which have different spectral properties and climatic effects. Our study also represents the first time temperature feedbacks have been investigated in relation to haze production in Archean Earth's atmosphere. Previous studies (Pavlov *et al.*, 2001b; Domagal-Goldman *et al.*, 2008; Haqq-Misra *et al.*, 2008) involving climate modeling have included the haze's impact on temperature but not corresponding temperature feedbacks on haze formation. Temperature feedbacks have significant impacts on the resultant hazes: as we discuss below, hazes produce stratospheric temperature inversions, and warmer atmospheres produce larger haze particles, so hazes generated by chemistry models without temperature feedbacks may not produce realistic results.

## 2. Models and Methods

To simulate the hazy Archean environment with boundary conditions consistent with recent geochemical constraints, we used a coupled 1-D photochemical-climate model we call Atmos and a 1-D radiative transfer model, SMART (Spectral Mapping Atmospheric Radiative Transfer).

### 2.1. Coupled photochemical-climate model

Our coupled photochemical-climate model, Atmos, is used to simulate Archean Earth's photochemistry and climate. To use Atmos, the photochemical model (which includes particle microphysics) is run first to generate an initial atmospheric state based on user-specified boundary conditions [gas mixing ratios or fluxes, the solar constant at 2.7 Ga (Claire *et al.*, 2012), the stellar spectral type, total atmospheric pressure, the initial temperature-pressure profile]. Then, the output files from the photochemical model for altitude, pressure, gas mixing ratios, haze particle sizes, and haze number densities are passed into the climate model. The climate model uses the photochemical model's solution as its initial conditions and runs until it reaches a converged state. It then feeds updated temperature and water vapor profiles back into the photochemical model. The models iterate back and forth in this manner until convergence is reached. An example of Atmos finding convergence can be seen in Fig. 1.

2.1.1. Photochemical model. The photochemical portion of the code is based on the 1-D photochemical code developed originally by Kasting *et al.* (1979), but the version we use here was significantly modernized and updated by Zahnle *et al.* (2006) and uses the haze formation scheme described by Pavlov *et al.* (2001b). It was modified by

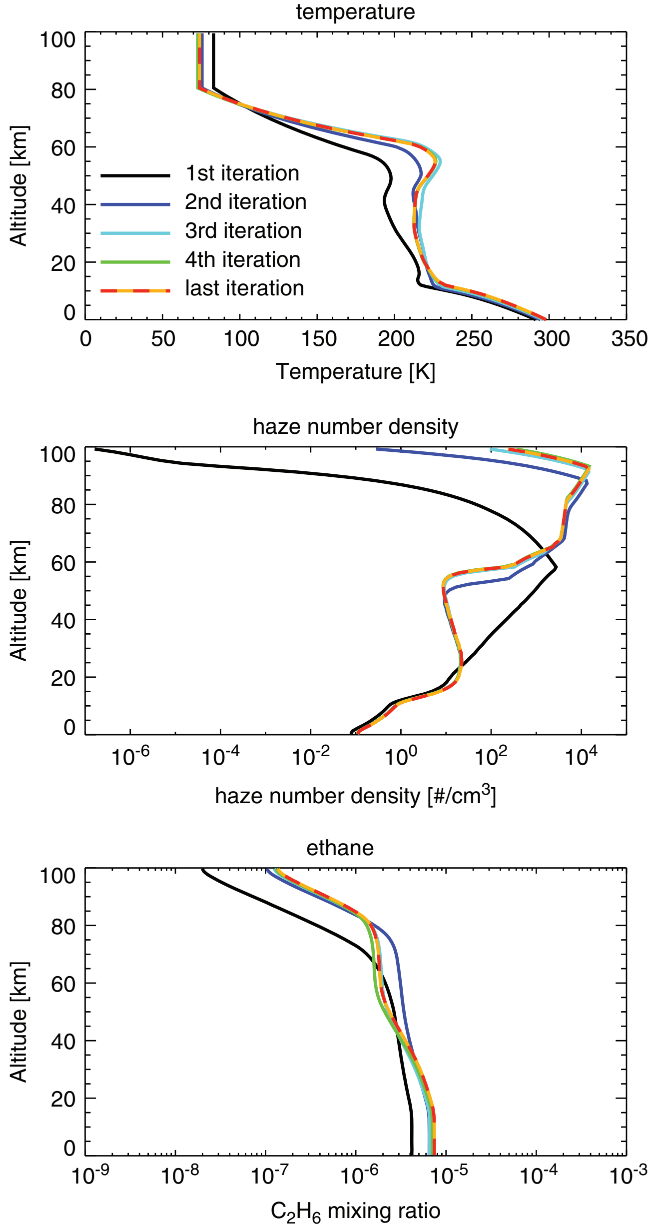

**FIG. 1.** Shown is an example of the Atmos model convergence process. This atmosphere, which has $CH_4/CO_2 = 0.17$ and $pCO_2 = 0.02$ (total pressure 1 bar) goes through five coupling iterations. The initial temperature profile it uses was stored from a previous similar atmosphere. Here we show the temperature, water, haze number density, haze particle radii, $C_2H_6$ profile, and $CH_4$ profile for each iteration of the coupled model.

E. Wolf to include fractal hydrocarbon hazes following the methods presented by Wolf and Toon (2010) and was first used to study fractal hazes on Archean Earth by Zerkle *et al.* (2012). Note that the version of the model used here can simulate atmospheres ranging from extremely anoxic ($pO_2 = 10^{-14}$) to modern-day $O_2$ levels (Zahnle *et al.*, 2006). Subsequent studies using this model or other versions of it to study fractal haze formation include those of Harman *et al.* (2013), Kurzweil *et al.* (2013), and Claire *et al.* (2014), with the latter two of these studies also derived from the same Zahnle *et al.* (2006) model branch used here. This model also has a long heritage of being used to study photochemistry in nonhazy atmospheres (*e.g.*, Kasting and Donahue, 1980; Pavlov and Kasting, 2002; Ono *et al.*, 2003; Segura *et al.*, 2003, 2005, 2007, 2010; Zahnle *et al.*, 2006; Grenfell *et al.*, 2007; Catling *et al.*, 2010; Domagal-Goldman *et al.*, 2011, 2014; Rugheimer *et al.*, 2013, 2015; Harman *et al.*, 2015; Schwieterman *et al.*, 2016).

The photochemical model parameters are as follows. Our model atmosphere is divided into 200 plane-parallel layers from the surface to 100 km, with a layer spacing of 0.5 km. We show a list of chemical reactions in our Supplementary Table S1 (Supplementary Data are available online at www.liebertonline.com/ast). Our Archean scheme includes 76 chemical species, 11 of which are short-lived (Supplementary Table S2). Short-lived species are considered in photochemical equilibrium (*i.e.*, their atmospheric transport is neglected) and are not part of the Jacobian solved self-consistently at each time step. The mixing ratio of each species is found by solving flux and mass continuity equations in each layer simultaneously using a reverse-Euler method, providing exact solutions at steady state. Vertical transport by molecular and eddy diffusion is included, and boundary conditions that drive the model can be set for each species at the surface and the top of the atmosphere. A $\delta$-2-stream method is used for radiative transfer (Toon *et al.*, 1989). Fixed isoprofiles are assumed for $CO_2$ and $N_2$ in the atmospheres considered here.

Similarly to the work of Zerkle *et al.* (2012), we set a fixed mixing ratio of $CH_4$ at the surface; the model then calculates the surface flux necessary to maintain this mixing ratio. Since haze formation scales with the $CH_4/CO_2$ ratio, we find this is the most straightforward way to explore haze thicknesses in our atmospheres. Note that when we discuss $CH_4/CO_2$ values in this study, these refer to the ratio at the planetary surface because $CH_4$ does not follow an isoprofile.

Aerosol formation follows the method used in Kasting *et al.* (1989) and described and updated in Pavlov *et al.* (2001b). Immediate precursors to haze particles are formed through the reactions $C_2H + C_2H_2 \rightarrow C_4H_2 + H$ and $C_2H + CH_2CCH_2 \rightarrow C_5H_4 + H$. Since the full chemical scheme that leads to aerosol formation is not well understood despite both laboratory and theoretical studies (*e.g.*, Hallquist *et al.*, 2009; Hicks *et al.*, 2015), it is assumed that $C_4H_2$ and $C_5H_4$ condense directly to haze particles (called HCAER and HCAER2 in Supplementary Table S1). In a real atmosphere, the molecules would be larger before aerosols condense, and back-reactions should occur, so this model may overestimate the rate of aerosol formation. Pavlov *et al.* (2001b) suggested that if the real aerosol formation rate was slower, the atmosphere would compensate by increasing the $CH_4/CO_2$ ratio, which would increase the polymerization rate. Further discussion of haze formation pathways and caveats of the approach we use here can be found in Section 4.4. The model's particles form initially with a radius of 0.001 $\mu$m. Each layer of the atmosphere has a monomodal size distribution calculated by comparing the coagulation lifetime to the particle removal lifetime via diffusion into another layer or by sedimentation. The aerosols can grow when the coagulation lifetime is longer than the lifetime for removal in a layer.

The maximum radius of a spherical haze particle (*i.e.*, a haze ''monomer'') is set to 0.05 $\mu$m, the same nominal value used by Wolf and Toon (2010) and similar to the size of the monomers of Titan's fractal haze aggregates (Rannou *et al.*, 1997; Tomasko *et al.*, 2008). Particles larger than this size are treated as fractal agglomerates of $n_{\mathrm{mon}}$ spherical monomers of radius $R_{\mathrm{mon}}$ that clump into a larger aggregate with an effective geometric radius $R_{\mathrm{f}}$ given by the relation

$$n_{\mathrm{mon}} = \alpha \left( \frac{R_{\mathrm{f}}}{R_{\mathrm{mon}}} \right)^{D_{\mathrm{f}}} \qquad (2)$$

Here, $\alpha$ represents a dimensionless constant of order unity, and $D_{\mathrm{f}}$ is the ''fractal dimension,'' which can take on values between 1 and 3. $D_{\mathrm{f}} = 3$ represents a spherical (nonfractal or classical Mie) particle, while $D_{\mathrm{f}} = 1$ represents a string of linearly chained monomers. Titan's fractal aggregates are thought to have a fractal dimension of about 2 on average for the aerosol population (Rannou *et al.*, 1997; Larson *et al.*, 2015). Note that the ''effective geometric radius'' we refer to above is used only to conceptualize the size of a fractal particle and does not indicate that we use Mie scattering for our fractal particles; with the exception of sub-monomer-sized particles ($R < 0.05$ $\mu$m) which remain spherical and thus Mie, we use the mean field approximation for fractal scattering physics for all particles (Botet *et al.*, 1997). The model's fractal production methods are discussed by Zerkle *et al.* (2012) (including their supplementary online information), where they were first implemented. Additional information about fractal particles and their geometry can be found in the works of, for example, Köylü *et al.* (1995) and Brasil *et al.* (1999). The mean field approximation we use for fractal scattering has been validated against scattering by silica fractal aggregates (Botet *et al.*, 1997) and Titan's hazes (Rannou *et al.*, 1997; Larson *et al.*, 2015).

As in the work of Wolf and Toon (2010), the fractal dimension of our particles varies from 1.5 to 2.4 for aggregate particles, and larger aggregates have a larger fractal dimension to account for folding as the particles coagulate. In general, compared to spherical particles, fractal particles produce *more* extinction in the ultraviolet (UV) but *less* in the visible and near infrared (NIR). In addition, fractals tend to be more forward scattering in the visible and NIR and more isotropically scattering in the UV compared to equal-mass spherical particles. Their weakened visible extinction and enhanced forward scattering compared to spherical particles means they produce less cooling since they scatter less incident sunlight back to space (see Fig. 3 in Wolf and Toon, 2010). Figure 2 shows the extinction efficiency ($Q_{\mathrm{ext}}$) and single-scattering albedo of different fractal particle sizes together with the haze optical constants we adopt in this study (Khare *et al.*, 1984a). A discussion of our choice of optical constants and comparison to others in the literature can be found in Section 4.5.

In the version of the photochemical model used here, we corrected an error relating to the calculation of the number of $C_5H_4$ molecules composing HCAER2 haze particles. Previously, the model calculated the number of molecules per HCAER2 particle inappropriately using the mass of $C_4H_2$ instead of $C_5H_4$. In addition, we added more particle sizes to the model's scattering grid, increasing the number from 34 particle sizes to 51, and we added options to use different monomer sizes and optical constants than the ones used here for our nominal haze study; how variation of these parameters impacts haze formation is a subject of future work. Gas mixing ratios at the surface can be more finely tuned than in previous versions of the model from the addition of a significant figure to the species boundary conditions input file.

The photochemical model is considered converged when redox is conserved and a re-run of the model using last run's output as initial conditions occurs quickly (*i.e.*, <50 time steps).

#### 2.1.2. Climate model.

Our climate model was originally developed by Kasting and Ackerman (1986). The model we use here has evolved considerably since its first incarnation, and versions of it have been applied in subsequent studies on varied topics such as the habitable zones for several stellar spectral types (Kopparapu *et al.*, 2013), the climate of early Mars (Ramirez *et al.*, 2013), the atmospheres of Earth-like planets around various stellar types (Segura *et al.*, 2003, 2005, 2010; Rugheimer *et al.*, 2013), clouds in exoplanet

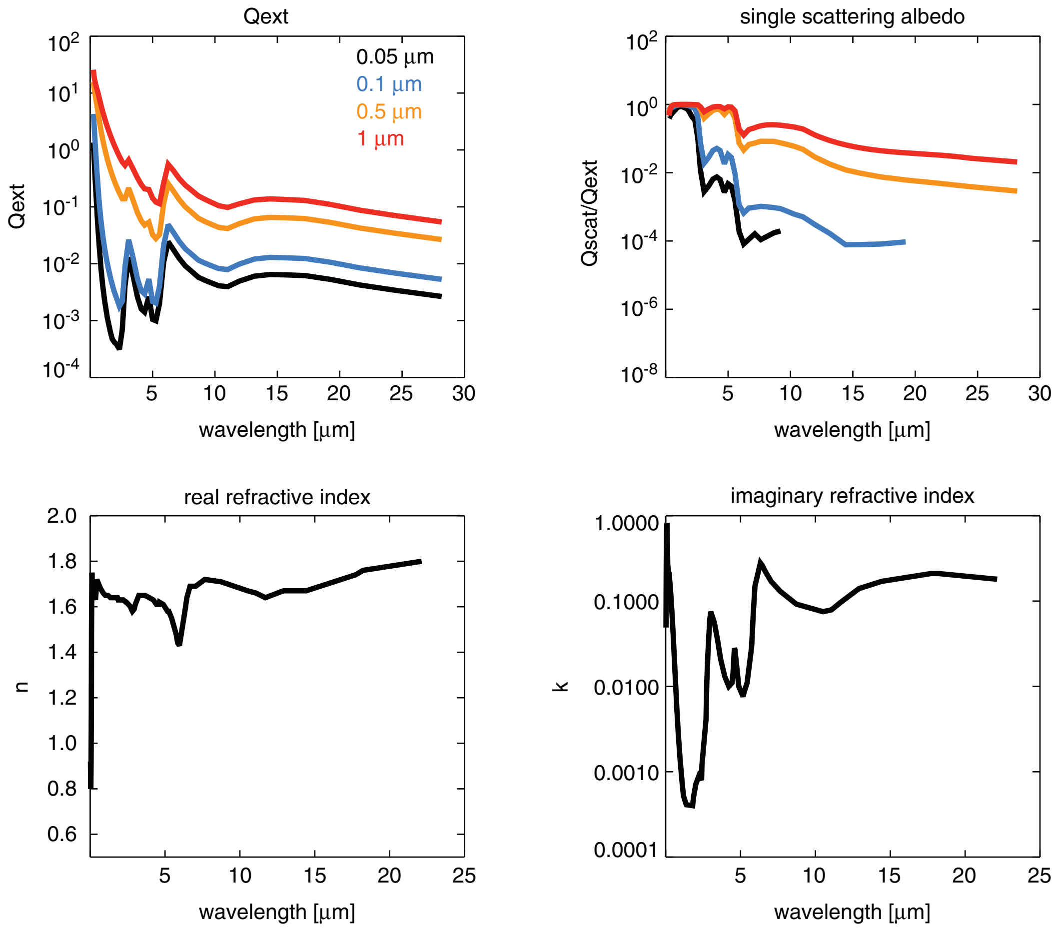

**FIG. 2.** The top panels present the extinction efficiency (Qext) and single-scattering albedo ( = Qscat/Qext) of four sizes of fractal hydrocarbon particles used in this study and in Wolf and Toon (2010). The spherical monomers comprising these particles are 0.05 $\mu$m in radius. The radii on the plot correspond to the radii of equivalent-mass spherical particles, and the fractal dimensions of these particles, from smallest to largest, are 3 (spherical), 1.51, 2.28, and 2.40. The number of monomers in these particles are 1, 8, 1000, and 8000. These particles tend to scatter and absorb light more efficiently at shorter wavelengths, and larger particles have flatter wavelength dependence for the scattering efficiency. Refractive indices, shown in the bottom panels, are presented from information in Khare *et al.* (1984a).

atmospheres (Kitzmann *et al.*, 2010, 2011a), and the climate of early Earth (Haqq-Misra *et al.*, 2008). The version we use here is based directly on that used by Kopparapu *et al.* (2013). It uses a correlated-*k* method to compute absorption by spectrally active gases ($O_3$, $CO_2$, $H_2O$, $O_2$, $CH_4$, and $C_2H_6$). This model has $CO_2$ and $H_2O$ correlated-*k* coefficients updated as described by Kopparapu *et al.* (2013). Our older $CH_4$ coefficients may overestimate the surface temperature by $\lesssim 5$ K at the $CH_4$ mixing ratios used here (Byrne and Goldblatt, 2015). However, as we discuss in Section 4.2, our model underpredicts the Archean temperature by about 2–5 K compared to 3-D climate models with more complete physics describing the planetary system, so these two effects may cancel each other out. The aforementioned gas profiles are passed to the climate model from the photochemical model when running in coupled mode. The net absorbed solar radiation in each layer of the atmosphere is computed using a $\delta$-2-stream multiple scattering algorithm (Toon *et al.*, 1989) spanning from $\lambda = 0.2$ to 4.5 $\mu$m in 38 spectral intervals. For net outgoing IR radiation, we use a separate set of correlated-*k* coefficients for each gas in 55 spectral intervals spanning wave numbers of 0–15,000 $cm^{-1}$.

We have made several modifications to the climate model used here. The model previously incorporated the spectral effects of spherical hydrocarbon particles, and it has been updated in our study to include fractal hydrocarbon scattering efficiencies using the mean field approximation of Botet *et al.* (1997) discussed previously. We have also updated the model so that haze profiles can be passed to it from an input file or by the photochemical code; in previous versions of the climate model, haze distributions were hard-coded and had to be edited manually. We corrected a discrepancy in the spacing between atmospheric layers in the routine that outputs coupling files for the photochemical model: our photochemical model layer spacing is 0.5 km, but a layer spacing of 1 km had been hard-coded. Coupling subroutines have been improved to be able to accept information about atmospheric pressure, stellar parameters, and haze parameters as input from the photochemical model. We also added options to turn ethane opacity and 1-D ice-albedo feedbacks (described in Section 4.1.1) on or off.

We have been unable to run the climate model to convergence using the same top-of-atmosphere pressure used for the photochemical model: the photochemical model extends to 100 km, but we have only been able to successfully run the climate model up to about 80 km for our 1 bar atmospheres. Thus, when temperature and water profiles are passed from the climate model to the photochemical model, they become isoprofiles above the top of the climate grid based on the highest-altitude temperature from the climate grid calculations. At these altitudes the atmosphere is thin, and the particles are very small; both of these effects lead to this portion of the atmosphere having little impact on radiative transfer and climate. We performed a sensitivity test of how the temperature at these altitudes affects the resultant haze distribution in the photochemical model, and the sizes of the largest haze particles produced by an atmosphere that becomes an 80 K isotherm above 80 km versus a 150 K isotherm differ by less than 5%. In the climate model, shifting the particles in Fig. 1 above 80 km down to lower altitudes alters the surface temperature by <0.5 K.

The climate model is considered converged when the change in temperature between time steps and change in flux out the top of the atmosphere are sufficiently small (typically on the order of $1 \times 10^{-5}$).

### 2.2. The SMART model

To generate synthetic spectra for the atmospheres we produce with Atmos, we feed outputs from the Atmos model (the temperature-pressure profile, gas mixing ratio profiles, and the haze particle profile), into the SMART code, a 1-D line-by-line fully multiple scattering radiative transfer model (Meadows and Crisp, 1996; Crisp, 1997). SMART has been validated against observations of multiple solar system planets (Robinson *et al.*, 2011; Arney *et al.*, 2014). The Line-by-Line Absorption Coefficients (LBLABC) code, a companion to SMART, creates line-by-line absorption files for input gas mixing ratios and temperature-pressure profiles using HITRAN 2012 line lists (Rothman *et al.*, 2013). SMART can also incorporate aerosols: as input, it requires ''cloud files'' with altitude-dependent opacities as well as the particle asymmetry parameter and the extinction, scattering, and absorption efficiencies ($Q_{\text{ext}}$, $Q_{\text{scat}}$, and $Q_{\text{abs}}$). For spherical particles (our small monomers), we use the code ''Miescat,'' to calculate these efficiencies using the indices of refraction measured by Khare *et al.* (1984a). For fractal hydrocarbon particles, we use scattering inputs from the Wolf and Toon (2010) photochemical study generated with the fractal mean field approximation (Botet *et al.*, 1997). Spherical particles use a full Mie phase function, while fractal particles employ a Henyey-Greenstein phase function (Henyey and Greenstein, 1941). To generate transit transmission spectra, we use the SMART-T model (Misra *et al.*, 2014a, 2014b). This version of SMART uses the same inputs as the standard code but simulates the longer path lengths and refraction effects associated with transit transmission observations.

To create SMART cloud files from Atmos haze outputs, we have written a script that bins the haze particles generated by the photochemical model into specified radii (also called particle ''modes'') while preserving the total mass of each atmospheric layer. The particle mode sizes we use span from 0.001 to 2 $\mu$m; larger particles do not exist in our atmospheres due to rainout. Spherical modes are $R = 0.001$, 0.005, 0.01, and 0.05 $\mu$m. Fractal modes are $R = 0.06$–2 $\mu$m with four modes between 0.06 and 0.1, 10 equally spaced modes between 0.1 and 1 $\mu$m, and 2 $\mu$m. In total, this represents 19 particle modes.

In each layer of the SMART cloud files, we include a mixture of two particle modes; the mass density contributed by the two modes is selected based on the distance in log space of the Atmos particle radius to each neighboring SMART size bin. For example, if Atmos produces a particle of radius 0.33 $\mu$m in a layer, the corresponding layer in SMART will include 0.3 and 0.4 $\mu$m particles each comprising 50% of the layer's mass. This binning is necessary because the photochemical model generates many dozens of finely differentiated haze particle radii, but SMART model run time with this many particle sizes is infeasible.

Once we have binned the Atmos particle radii to our SMART size grid, we must compute the total optical depth from each particle mode at a reference wavelength in each atmospheric layer. We arbitrarily select 1 $\mu$m as our reference wavelength. Optical depth in a layer, $\tau$, from particles of a given radius, $R$, depends on the number density of particles per particle size, $n(R)$, the thickness of the atmospheric layer, $z$, and the wavelength-dependent extinction efficiency, $Q_{\text{ext}}$:

$$\tau = z \int_{R_{\min}}^{R_{\max}} \pi r^2 Q_{\text{ext}}(\lambda, R) n(R) dR \tag{3}$$

For fractal particles ($R > 0.05$ $\mu$m), the cross-sectional area and the corresponding extinction efficiencies are computed relative to the radius of an equal-mass spherical particle, following the conventions of mean-field approximation (Botet *et al.*, 1997). Spherical particles in SMART are binned according to log-normal size distributions using the radii mentioned previously and a mode standard deviation of 1.5, which is realistic for an aerosol distribution (Tolfo, 1977). For fractal particles, we use a monodisperse distribution, the same size distribution used to compute our inputs from the previous Wolf and Toon (2010) fractal haze study and the same distribution used in the Atmos model.

### 2.3. Model inputs

In the photochemical model, we set a haze monomer density of 0.64 g/cm$^3$, which is consistent with the laboratory results of Trainer *et al.* (2006) for early Earth. This density is used in the model to calculate the masses of haze particles and is updated from the value of 1 g/cm$^3$ used by previous studies employing our photochemical model. Hörst and Tolbert (2013) measured a similar effective particle density, 0.65 g/cm$^3$, for a 0.1% $CH_4$ haze experiment using a UV lamp. One-tenth percent $CH_4$ is consistent with the atmospheres we simulate, although the Hörst and Tolbert hazes were Titan analog simulants lacking the $CO_2$ present in the Trainer *et al.* experiments. We apply a Manabe/Wetherald relative humidity model for the troposphere (Manabe and Wetherald, 1967) with a surface relative humidity of 0.8 in both the climate and photochemistry models. This humidity parameterization is further described by Pavlov *et al.* (2000). Our Archean simulations use the solar constant at 2.7 Ga ($0.81 = S/S_0$, where $S_0$ is the modern solar constant and $S$ is the solar constant at 2.7 Ga) modified by a wavelength-dependent solar evolution correction (Claire *et al.*, 2012). We chose this time because it corresponds to the age of the constraints on $CO_2$ used by our study (Driese *et al.*, 2011). We set the mixing ratio of $O_2$ at the surface to $1.0\times10^{-8}$, consistent with the Zerkle *et al.* (2012) study. These conditions reflect the time period after the evolution of oxygenic photosynthesis but prior to Earth's GOE in which substantial biogenic fluxes of both oxygen and methane would have vented into a predominantly reducing atmosphere (Claire *et al.*, 2014). Unless otherwise specified, the surface albedo used by the climate model is 0.32. This includes the effect of clouds, which is standard in this 1-D treatment (Kopparapu *et al.*, 2013) and is the albedo that reproduces the average temperature of present-day Earth (288 K) with modern atmospheric conditions. Of course, the true cloud distribution on Archean Earth is unknown, and clouds may have had important climatic effects on our early planet (Goldblatt and Zahnle, 2011). The solar zenith angles (SZAs) used in the climate and photochemical models were chosen to best represent globally averaged behavior of the physics in each specific model, which Segura *et al.* (2003) found as SZA = 45° in the photochemical model and SZA = 60° in the climate model. These zenith angles are both tuned to reproduce modern-day Earth's average chemical profiles and climate, respectively.

For our SMART spectral simulations, our nominal spectra assume an ocean surface albedo (McLinden *et al.*, 1997). In cases where an icy surface is used, we use an albedo from the USGS Digital Spectral Library (Clark *et al.*, 2007). Our solar spectrum was modeled by Chance and Kurucz (2010) and was scaled by the solar evolution model (Claire *et al.*, 2012) mentioned previously. The SZA is set at 60° for the reflection spectra, which approximates a planetary disk average near quadrature (planet half illuminated to the observer).

## 3. Results

In this section, we first describe the climate results from Atmos. Following this, we quantify the strength of a hazy UV shield for surface organisms, and we show and describe the spectral consequences of this haze in reflected light and transit transmission spectroscopy.

Recent paleosol measurements have constrained the $CO_2$ partial pressure ($pCO_2$) in the Archean at 2.7 Ga to be between 0.0036 and 0.018 bar [10–50× the present atmospheric level (PAL)] (Driese *et al.*, 2011), while recent estimates of Archean surface pressure ($P_{surf}$) are consistent with values as low as 0.5 bar (Som *et al.*, 2012; Marty *et al.*, 2013). We simulated four types of atmospheres that span these constraints to examine a range of conditions: $pCO_2 = 0.01$ and $P_{surf} = 1$ bar of total pressure (Case A), $pCO_2 = 0.018$ and $P_{surf} = 1$ bar (Case B), $pCO_2 = 0.01$ and $P_{surf} = 0.5$ bar (Case C), and lastly, $pCO_2 = 0.0036$ and $P_{surf} = 0.5$ bar (Case D). These are summarized in Table 1. The haze thickness scales with the $CH_4$ abundance relative to $CO_2$, so we investigated a range of $CH_4$ levels for each of these atmospheres. In the sections below, we refer to these Case A–D planets. Figure 3 shows an example of the atmospheric profiles for several gases in atmospheres with two different $CH_4/CO_2$ ratios (0.1 and 0.2), plus the haze number density profiles scaled to fit on the same *x* axis. The insignificant haze present in the $CH_4/CO_2 = 0.1$ atmosphere is spectrally indistinguishable from an atmosphere with no haze. The larger amounts of $CH_4$, $C_2H_6$, and $H_2O$ at higher altitudes in the $CH_4/CO_2 = 0.2$ atmosphere illustrate how the haze can shield these gases from photolysis.

Table 1. Atmosphere Parameters for Cases A–D

| | *Case A* | *Case B* | *Case C* | *Case D* |
|---|---|---|---|---|
| $pCO_2$ (bar) | 0.01 | 0.018 | 0.01 | 0.0036 |
| $P_{surf}$ (bar) | 1 | 1 | 0.5 | 0.5 |

Our results presented here required about 60 Atmos model runs. In total, we ran about twice this number for model debugging and testing. Each coupled Atmos run can take between 3 and 15 h depending on how many coupling iterations are required. Note that the run time for the climate model scales nonlinearly with the number of radiatively active gases: a model run that takes less than 20 min without $CH_4$ or $C_2H_6$ will require well over an hour with both of these gases turned on. All the results presented here, except as noted in Section 4, were generated with both $CH_4$ and $C_2H_6$.

Note that in the context of the results presented here, a ''thick'' haze refers to the haze at a $CH_4/CO_2$ ratio $\sim 0.2$.

### 3.1. Hazy climates

We find that hazy Archean climates were cold but most likely habitable (Fig. 4). Previous 1-D climate modeling efforts assumed that planets with globally averaged surface temperatures ($T_{GAT}$, which is equivalent to our 1-D surface temperature, $T_{surf}$) below 273 K will experience runaway glaciation (*e.g.*, Domagal-Goldman *et al.*, 2008; Haqq-Misra *et al.*, 2008). However, more recent 3-D studies have shown that Archean Earth can maintain an open ocean fraction of >50% for $T_{GAT} \geq 260$ K and an equatorial open ocean belt for $T_{GAT} \geq 248$ K (Wolf and Toon, 2013; Charnay *et al.*, 2013). Furthermore, Abbot *et al.* (2011) argued that ocean open belts can remain climatologically stable, even if the ice latitude is reduced to 5–15°. Since a planet with any nonzero fraction of open ocean is habitable, we regard these updated globally averaged temperatures—all of which are significantly below freezing—to be more realistic habitability thresholds than 273 K. We adopt $T_{GAT} \geq 248$ K as our habitability threshold here.

Figure 4 shows that when haze reaches a threshold thickness, further increases in $CH_4$ result in rapid increases in haze thickness and a corresponding steep falloff in surface temperature. However, at higher $CH_4/CO_2$ ratios, the haze thickness (and the surface temperature) stabilizes because UV self-shielding inhibits methane photolysis, shutting down haze formation. Thus, we find there is a maximum haze optical thickness—and a minimum temperature from haze-induced cooling—for each atmosphere. Interestingly, this negative feedback haze self-shielding appears to prevent catastrophic cooling. Note that even using the conventional habitability threshold of 273 K, Cases A–C have a hazy solution space where $T_{surf} > 273$ K, and Case B stabilizes at $T_{surf} = 274$ K with its thickest haze. By using the updated habitability threshold of $T_{surf} > 248$ K, all our cases even with thick hazes are habitable. Table 2 summarizes these results and includes a sensitivity test of the ice-albedo effect, described below.

Although the cold climates we have simulated are ''habitable'' in the sense that they have open ocean, a cold climate with extended ice caps ($T_{surf} < 273$ K) from a thick haze may

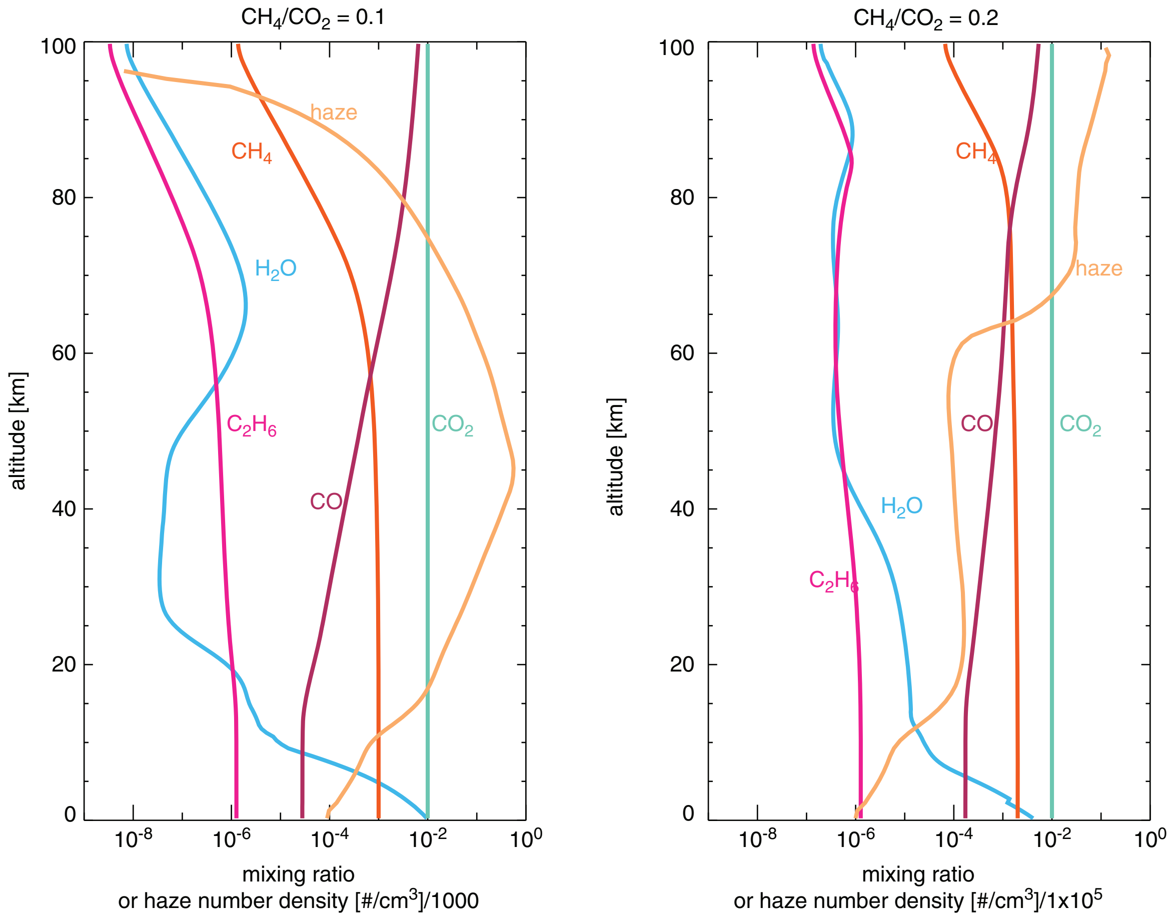

**FIG. 3.** The gas profiles for $H_2O$, $CH_4$, CO, $CO_2$, and $C_2H_6$ for planets with $pCO_2 = 0.01$ bar for $CH_4/CO_2 = 0.1$ (on the left) and $CH_4/CO_2 = 0.2$ (on the right). Also shown are the profiles for the haze particle number density (in pale orange). The $CH_4/CO_2 = 0.1$ haze profile is divided by 1000, and the $CH_4/CO_2 = 0.2$ haze profile is divided by $1 \times 10^5$ in order to plot it on the same axis as the gases. The profiles in the right panel show larger amounts of $CH_4$, $H_2O$, and $C_2H_6$ above 60 km in altitude and illustrate how haze-induced shielding can prevent photolysis of these gases. The sharp decrease in haze particle number density between 60 and 70 km in the right panel shows where fractal coagulation occurs. The atmosphere above the fractal coagulation region is populated by spherical submonomer particles.

be consistent with a reported glaciation event at 2.9 Ga (Young *et al.*, 1998) as a previous study has suggested (Domagal-Goldman *et al.*, 2008). Later purported hazy periods around 2.7 Ga (Kurzweil *et al.*, 2013; Izon *et al.*, 2015) and between 2.65 and 2.5 Ga (Zerkle *et al.*, 2012) are not associated with glaciations and may be consistent with the thinner-haze solution space of Cases A and C or even the thickest haze solution space of the warmer Case B.

### 3.1.1. Ice-albedo feedback.

To test how ice-albedo-feedbacks can affect our retrieved temperatures, we tested the influence of these feedbacks on the minimum temperatures reached by our four cases by parameterizing our model's 1-D surface albedo (*A*) by the relation (based on the results of Charnay *et al.*, 2013) to include the albedo effect of clouds and ice as a function of the globally averaged temperature:

$$A(T_{\mathrm{GAT}}) = 0.65 + (0.3 - 0.65) \times \left( \frac{T_{\mathrm{surf}} - 240}{290 - 240} \right)^{0.37} \quad (4)$$

As stated above, the surface albedo used by our nominal model is 0.32. The surface albedos for the Case A, B, C, and D minimum temperatures with this ice-albedo parameterization are 0.39, 0.35, 0.39, and 0.45. The climate model was run to convergence starting with the solution for the minimum stabilized temperature for each case (*i.e.*, when the haze becomes self-shielding and reaches maximal thickness) as a test of the sensitivity of our minimum temperatures to ice-albedo feedbacks. The temperatures of planets A, B, C, and D with ice-albedo feedbacks are 257, 271, 257, and 241 K, a decrease of 3–10 K compared with simulations with the nominal albedo. The Bond albedos produced in these cases including haze are 0.26, 0.24, 0.26, and 0.29.

These ice-albedo temperatures may be underestimates because once haze forms, deposition of dark hydrocarbons onto ice-covered areas will lower the albedo of the ice. This decreased ice albedo may then melt the ice, reverting parts of the surface back to ocean water. Because haze absorbs strongly at blue wavelengths, the radiation that reaches the surface under a haze would have a higher proportion of longer, redder wavelengths compared to shorter, bluer

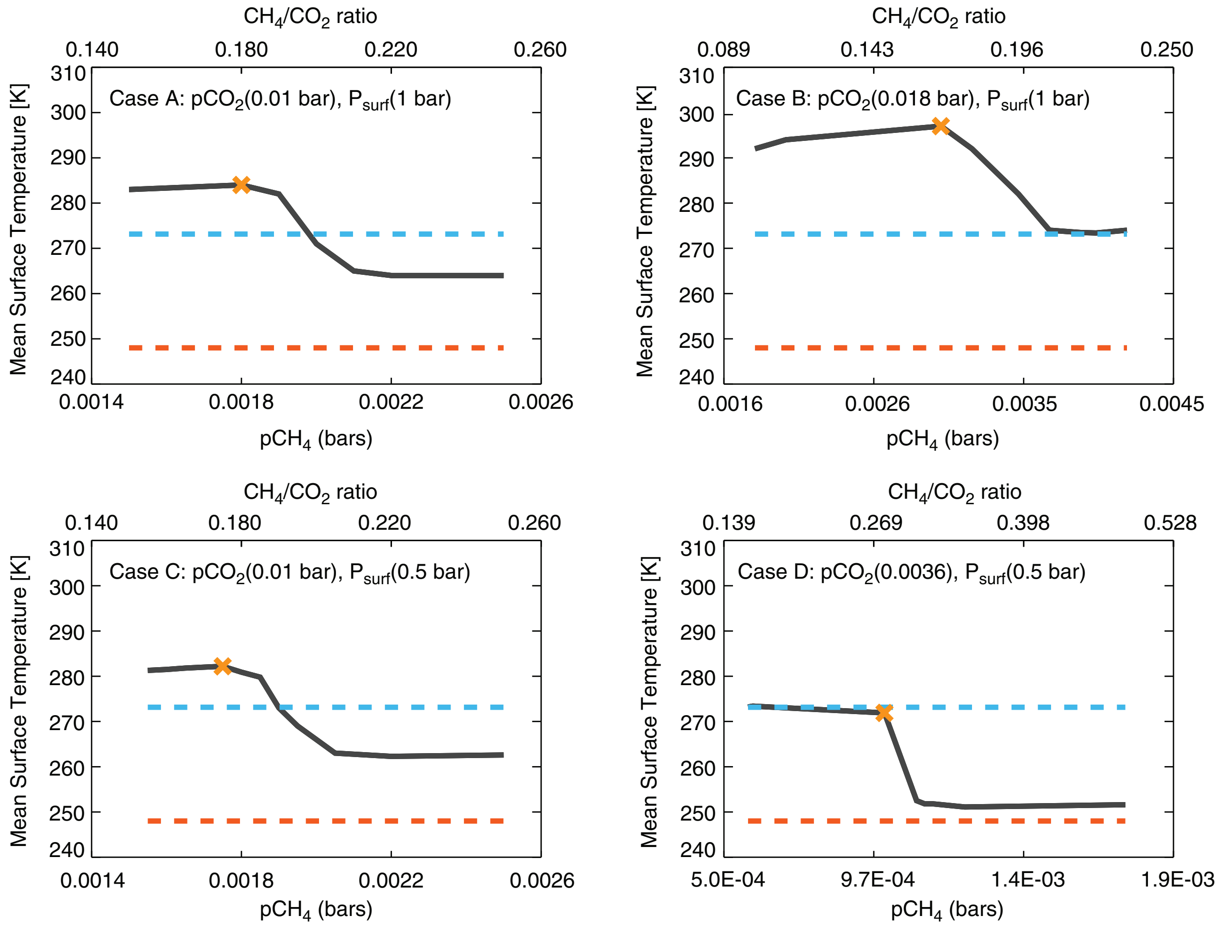

**FIG. 4.** Mean surface temperatures as a function of $CH_4$ for Archean Cases A–D. The dashed blue line shows the freezing point of water (273 K), and the dashed orange line marks our lower threshold of habitability (248 K) for an equatorial ocean belt (Charnay *et al.*, 2013). The X in each panel indicates the initiation of haze-induced cooling.

wavelengths. While ice is very reflective at visible wavelengths, it becomes more absorbing at wavelengths $>0.7\,\mu$m, changing the true ice-albedo parameterization. Because of this, planets orbiting stars emitting a high proportion of radiation at NIR wavelengths are harder to freeze (Shields *et al.*, 2013). Additionally, stratospheric and mesospheric circulation patterns on Earth presently impact high-altitude aerosol distributions by transporting particles preferentially to the poles (Bardeen *et al.*, 2008). In this case, the climatic impact of haze could be reduced with warmer surface temperatures at the equator. On the other hand, hazes can also act as cloud condensation nuclei, enhancing cloud formation (Hasenkopf *et al.*, 2011). This might lead to cooling of the planet or even warming depending on cloud particle size and the altitude—and therefore temperature—of the cloud layer (Goldblatt and Zahnle, 2011). A complete treatment of the impact of ice-albedo feedback, haze deposition, haze circulation, and cloud feedbacks is left to future General Circulation Model (GCM) studies better equipped to deal with these inherently 3-D issues.

Table 2. Temperature Results for Cases A–D

| | *$CH_4/CO_2$ to initiate haze formation* | *Maximum $T_{surf}$ without haze (K)* | *Stabilized $T_{surf}$ with haze (K)* | *$T_{surf}$ with ice-albedo feedback (K)* |
|---|---|---|---|---|
| Case A | 0.18 | 284 | 263 | 257 |
| Case B | 0.15 | 299 | 274 | 271 |
| Case C | 0.19 | 282 | 262 | 257 |
| Case D | 0.28 | 273 | 251 | 241 |

### 3.1.2. Temperature feedbacks on haze production.

As the haze gets optically thicker, absorption of UV photons produces an atmospheric temperature inversion (Fig. 5) similar to that produced by ozone in the modern atmosphere. We find there is a relationship between the size of the haze particles generated and the temperature of the atmosphere. To isolate the effect, we tested haze production by the photochemical model using two completely isothermal temperature profiles of 200 and 250 K with all other parameters held constant (Fig. 6). The largest particles produced by the 250 K atmosphere have a geometric radius of $0.8\,\mu$m compared to $0.65\,\mu$m radius particles for the 200 K atmosphere. In the photochemical model, when the coagulation timescale ($\tau_{coag}$) is shorter than the timescale for removal in an atmospheric layer, the particles can grow. As temperature increases, $\tau_{coag}$ decreases since particles moving faster collide more frequently (Tolfo, 1977). In the hotter atmosphere, $\tau_{coag}$ is smaller than $\tau_{sed}$ through most of the atmospheric column.

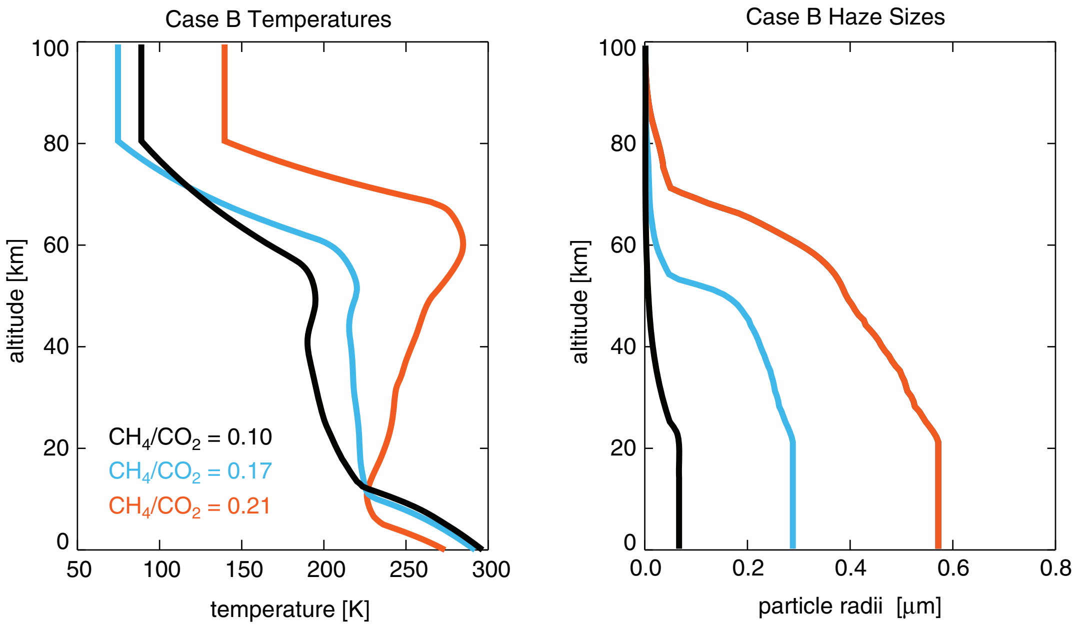

**FIG. 5.** The left panel presents the temperature profiles of three $CH_4/CO_2$ ratios for the Case B planet. Note the strengthening temperature inversion as the $CH_4$ content of the atmosphere increases. The right panel shows the size of haze particles produced in these three atmospheres, showing the dependence of haze particle size on temperature. From least to most $CH_4$ (and thinnest to thickest haze), the particles reach a maximum radius of 0.067, 0.28, and 0.57 $\mu$m. Note that the temperature profiles become isothermal at the top of the climate model grid when transferred to the larger photochemical model grid.

### *3.2. UV shielding*

The impact of these hazes on the biosphere goes beyond temperature reduction: their fractal nature makes them strong absorbers at short wavelengths and therefore a potential shield against damaging UV radiation for the anoxic Archean (Wolf and Toon, 2010), which would have received significantly more UV at the surface than the planet today (Rugheimer *et al.*, 2015). DNA damage is most acute in the UVC ($\lambda < 0.28\ \mu$m) wavelength range (Pierson *et al.*, 1992; Dillon and Castenholz, 1999), but in the modern atmosphere, UVC is fully blocked by $O_2$ and ozone. For the haze-free Case B atmosphere ($CH_4/CO_2 = 0.1$), our models calculate the flux of UVC at the surface as about 0.93 W/m$^2$ for a SZA of 60° and 2.62 W/m$^2$ for SZA = 0°. Both of these values are sufficient for sterilization (Pierson *et al.*, 1992). In contrast, the surface UVC flux under a haze for Case B ($CH_4/CO_2 = 0.21$) would have been about 0.03 W/m$^2$ for SZA = 60° and 0.22 W/m$^2$ for SZA = 0°. We compare these values to the tolerances of *Chloroflexus aurantiacus* (Pierson *et al.*, 1992), a deep-branching, mat-forming anoxygenic phototroph with UV resistance that has been studied as an analogue for Archean phototrophs. Our SZA = 60° flux, 0.03 W/m$^2$, is low enough to allow growth of *Chloroflexus aurantiacus* over the length of a day in the late Archean [about 18–19 h for a day-night cycle; Denis *et al.* (2002)]. Our SZA = 0° flux, 0.22 W/m$^2$, is

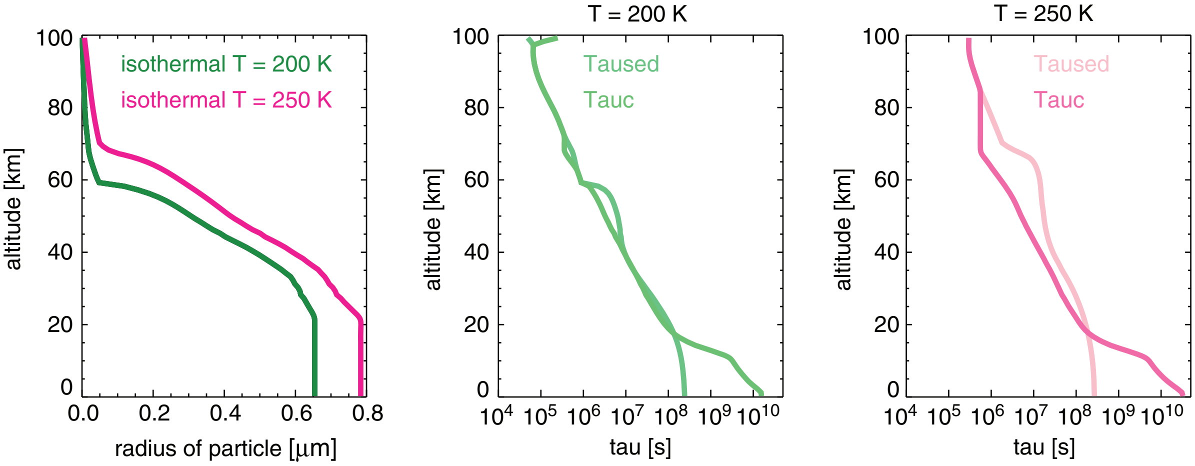

**FIG. 6.** The haze particle sizes for two completely isothermal atmospheres together with the coagulation and sedimentation timescales for these atmospheres.

Table 3. The UV Fluxes at the Planetary Surface for Several Overlying Atmospheres

| | *Modern Earth* | *Proterozoic 1% PAL $O_2$* | *Proterozoic 0.1% PAL $O_2$* | *Case B $CH_4/CO_2=0.1$* | | | *Case B $CH_4/CO_2=0.17$* | | | *Case B $CH_4/CO_2=0.2$* | | |
|---|---|---|---|---|---|---|---|---|---|---|---|---|
| | | | | *H* | *H+C* | *H+S* | *H* | *H+C* | *H+S* | *H* | *H+C* | *H+S* |
| SZA = 0° | | | | | | | | | | | | |
| UVA | 70.5 | 59.1 | 59.3 | 55.5 | 50.84 | 38.1 | 48.8 | 44.3 | 33.2 | 22.8 | 20.2 | 15.0 |
| UVB | 2.49 | 6.18 | 10.6 | 10.2 | 9.32 | 7.26 | 8.11 | 7.38 | 5.76 | 2.19 | 1.96 | 1.52 |
| UVC | ~0 | 0.00764 | 2.03 | 2.62 | 2.41 | 1.95 | 1.87 | 1.71 | 1.38 | 0.216 | 0.196 | 0.158 |
| SZA = 60° | | | | | | | | | | | | |
| UVA | 28.9 | 24.4 | 24.5 | 23.0 | 18.42 | 13.2 | 17.7 | 14.4 | 10.4 | 4.93 | 4.14 | 3.00 |
| UVB | 0.446 | 1.77 | 3.90 | 3.82 | 3.29 | 2.51 | 2.51 | 2.18 | 1.67 | 0.337 | 0.29 | 0.22 |
| UVC | ~0 | $7.29\times10^{-4}$ | 0.565 | 0.932 | 0.841 | 0.673 | 0.512 | 0.471 | 0.376 | 0.0318 | 0.0290 | 0.0252 |

All values quoted have units of W/m$^2$. The solar constant for geological times has been scaled according to Claire *et al.* (2012) at 2.5 Ga for the Proterozoic and 2.7 Ga for the Archean. All calculations have been performed assuming that the Sun is either directly overhead (SZA = 0°) or at a SZA of 60°. There are three Archean UV fluxes per UV band and $CH_4/CO_2$ ratio: they refer to haze only (labeled "H"), haze plus cirrus cloud (labeled "H + C"), and haze plus stratocumulus cloud (labeled "H + S"). The Modern Earth and Proterozoic atmospheres are cloud- and haze-free. UVA spans $\lambda = 0.315$–$0.400\,\mu$m. UVB spans $\lambda = 0.280$–$0.315\,\mu$m. UVC is $\lambda < 0.280\,\mu$m.

naturally worse but does not cause immediate sterilization of *Chloroflexus aurantiacus*, allowing modest growth for roughly 10 h. In a real atmosphere, the UV flux will change with SZA, but it will not exceed the SZA = 0° flux. At latitudes where the SZA is never 0°, UV survival prospects are better, although these higher latitudes may be icy for our cold planets. Under an Archean haze, it is possible that organisms similar to *Chloroflexus aurantiacus* with robust UV protection mechanisms could have lived at or near the planet's surface. We summarize the UV protection of several types of atmospheres, including ones with water clouds that can confer additional UV protection, in Table 3. This table only includes Case B, but the other cases produce similar results for UV shielding because they have similar optical thicknesses.

Possibly, an Archean haze aided the survival of life at or near the surface of our early planet. There is evidence that Archean stromatolitic communities lived in inter- and supratidal zones (Allwood *et al.*, 2006; Noffke and Awramik, 2013) experiencing frequent, sometimes extended, exposure to the surface environment, and it has been suggested that microbial mats existed on land as early as 2.7–2.6 Ga (Watanabe *et al.*, 2000). Interestingly, this interval overlaps with periods when haze has been proposed for the Archean atmosphere (Zerkle *et al.*, 2012; Kurzweil *et al.*, 2013; Izon *et al.*, 2015).

It has widely been assumed that Proterozoic Earth's surface received less UV than the Archean due to the rise of oxygen ($O_2$) and ozone (*e.g.*, Rugheimer *et al.*, 2015), but a recent

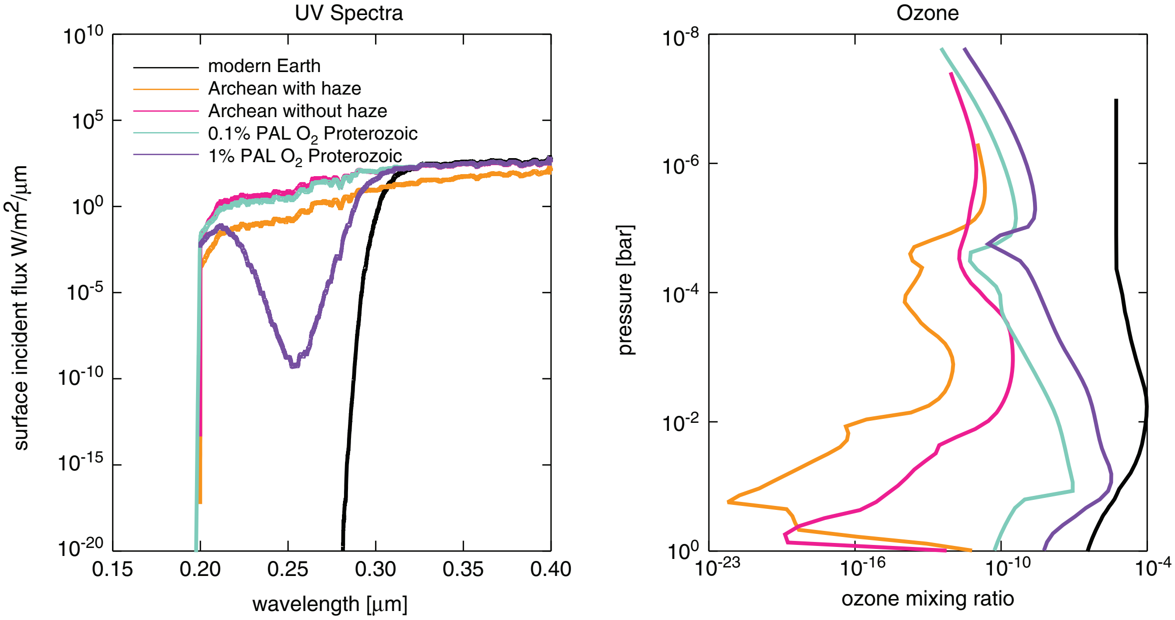

**FIG. 7.** Shown are surface UV spectra (left) and ozone column abundances (right) for Archean, Proterozoic, and modern Earth atmospheres. A modest amount of $O_2$ in the Proterozoic (1% PAL) produces a stronger UV shield than the Archean haze, but the haze shown here cuts out more UVA (320–400 nm) and UVB (280–320 nm) radiation than ozone in all situations. The haze can produce a stronger UV shield compared to the low $O_2$ atmosphere (0.1% PAL) proposed recently by Planavsky *et al.* (2014) for our atmospheric assumptions.

study of chromium isotopes suggests that the Proterozoic $O_2$ mixing ratio was, at most, 0.1% PAL (Planavsky *et al.*, 2014). We tested the strength of an ozone UV shield generated by our photochemical model under these low-oxygen conditions against the strength of our hazy UV shield. For the Proterozoic atmospheres, we tested ozone generation at 0.1% and 1% PAL $O_2$ levels (Fig. 7) with $pCO_2$ fixed at 0.01 bar and $pCH_4$ at 0.0003 bar. Total pressure is set to 1 bar at the surface. According to these assumptions, Proterozoic Earth with 0.1% PAL $O_2$ would have received 0.57 W/m$^2$ of UVC at the surface, so in this case, the Archean hazy UV shield was stronger. Note also that haze is a better shield against UVA ($\lambda = 0.315–0.400\,\mu$m) and UVB ($\lambda = 0.280–0.315\,\mu$m) than ozone or $O_2$.

### 3.3. Spectra

The strong interaction of haze with radiation means hazes can impact the exoplanet spectra that future space-based telescopes will attempt to detect. In Fig. 8, we show reflectance, thermal emission, and transit transmission spectra for our nominal Case B with an ocean surface; the other cases produce similar spectra as discussed below. Our predicted spectra of hazy Archean Earth show diagnostic absorption features from $H_2O$, $CO_2$, $CH_4$, $C_2H_6$, CO, and from the haze itself. These features are labeled in Fig. 8, and another way to show where these gases and the haze absorb is presented in Figs. 9 and 10 for reflectance and transit transmission spectra, respectively. Figures 9 and 10 were

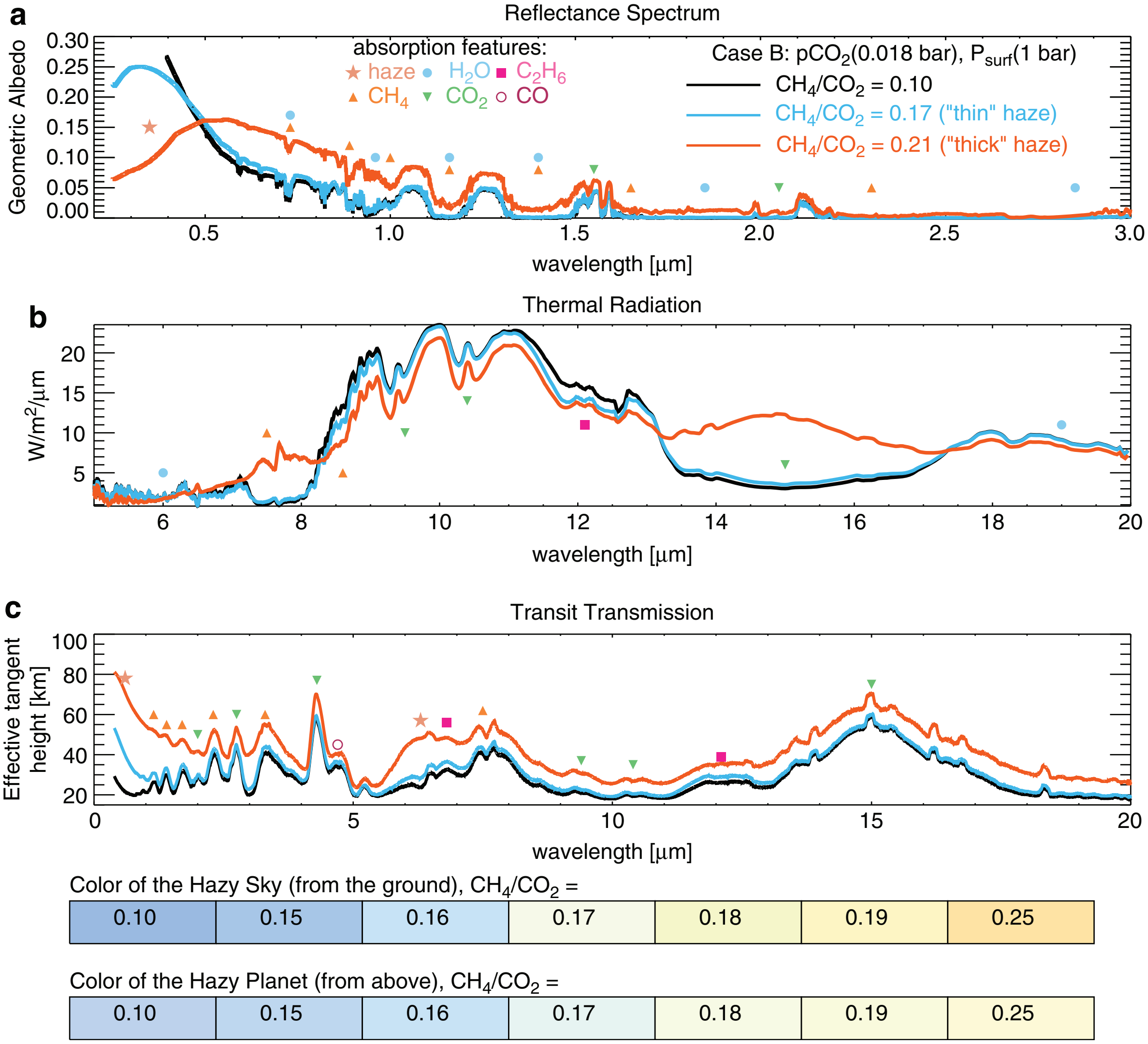

**FIG. 8.** Shown here are spectra for Case B. Haze and gas absorption features are labeled with the symbols indicated. (**a**) At short wavelengths in direct imaging, haze absorption decreases the planet's brightness; scattering brightens the planet at longer wavelengths. (**b**) Thermal emission from the hot stratosphere of the thickest haze planet ($CH_4/CO_2 = 0.21$) fills in absorption bands near 8 and 16 $\mu$m. (**c**) The *y* axis shows the effective transit height above the planet's surface that light is able to penetrate, and absorption features are inverted compared to (a) and (b) due to an increase in the effective planet radius during transit resulting from an increase in absorption at these wavelengths. The bottom section shows the approximate color of the hazy sky and planet. Sky colors are computed using the diffuse radiation spectrum at the ground. "Effective tangent height" refers to the minimum altitude above the planet's surface that light is able to penetrate on transit transmission paths.

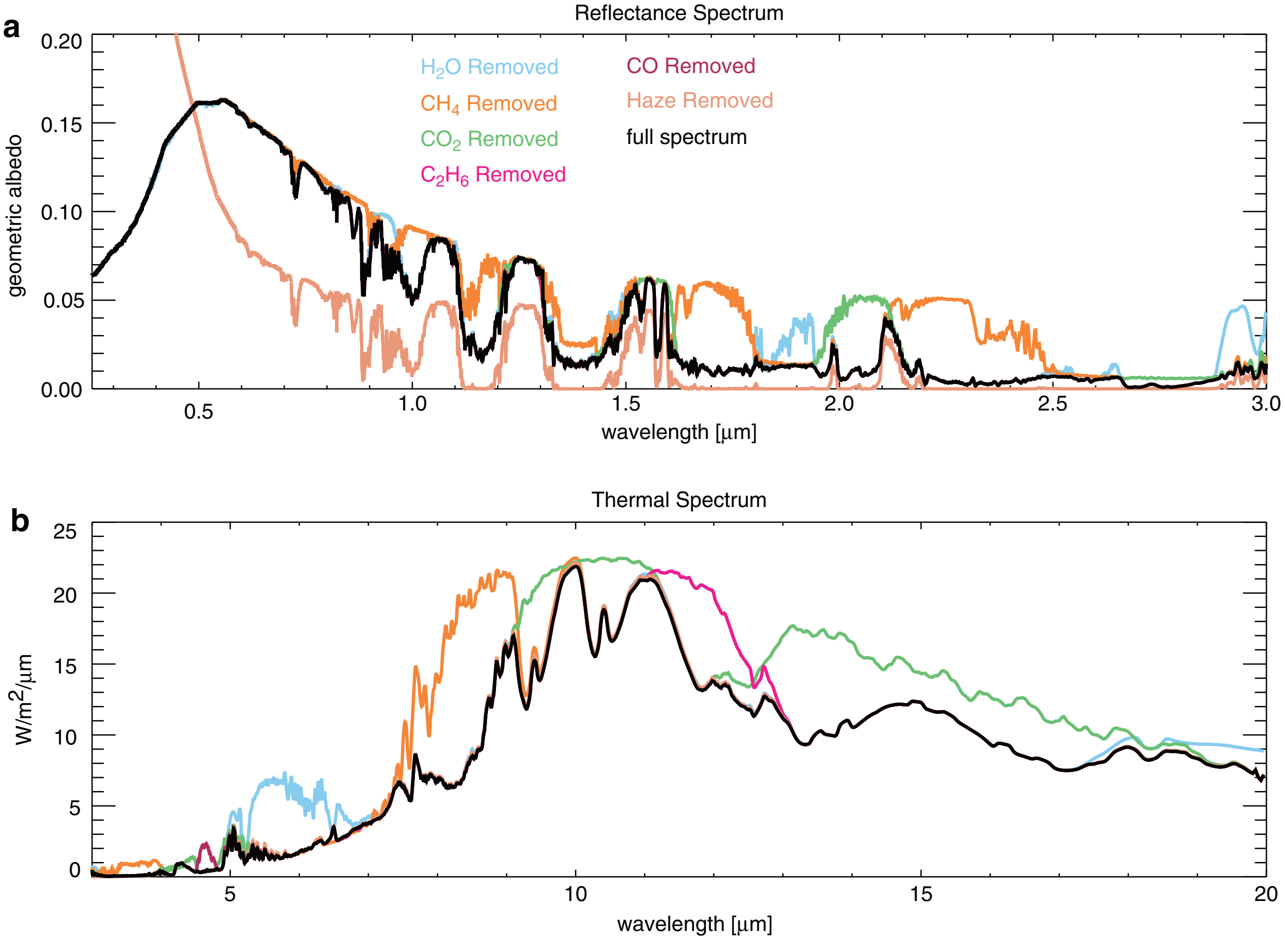

**FIG. 9.** A reflectance spectrum for a hazy Case B planet in the visible and NIR (**a**) and mid-IR (**b**) is presented with gases and the hydrocarbon haze removed to show where each spectral component interacts with radiation. The full spectrum is shown in black. Places where the black spectrum deviates from the colored spectra indicate where each gas or haze absorbs. For example, the green line shows a spectrum where $CO_2$ is omitted, and a strong $CO_2$ feature is present near 15 $\mu$m in (B) as shown by the deviation of the green spectrum from the black spectrum. At some wavelengths, gas and haze absorptions are complex to detangle because multiple species are absorbing: in these cases, the key on Fig. 8 will indicate which gases are the dominant absorbers in a region.

produced by systematically removing each gas or the haze; in places where a given species absorbs, the original spectrum differs from those with the absorbers removed. To consider the spectral effect of haze without contamination from other atmospheric aerosols, the spectra in this section do not include water clouds, even though cloud albedo is implicit in the parameterization of the Atmos model's surface albedo. This makes the albedos of the planets whose spectra are shown in this section darker than those in the Atmos parameterization. However, since clouds have a major impact on the planet's spectral appearance and albedo (*e.g.*, Kitzmann *et al.*, 2011b), we show spectra with water clouds included in Section 3.3.1. The best way to treat the climatic and spectral impact of both clouds and haze would be in a fully coupled 3-D climate-photochemical model that fully considers radiative and photochemical effects of cloud and haze particles, but this is outside the scope of this work. To our knowledge, such a 3-D model does not yet exist, but its development would be useful for the comprehensive treatment of this problem.

In reflected light (Fig. 8a), the broad UV absorption feature reddens the color of the planet by masking the short-wavelength reflectivity due to Rayleigh scattering. See the bottom section of Fig. 8 for the estimated color of the planet to the eye. The planet colors were calculated using the ‘‘Spectral Color Spreadsheet'' from brucelindbloom.com with the same method used by Charnay *et al.* (2015) for GJ 1214b. A spectrum can be input to the calculator, which then outputs RGB values. While these colors should be understood as approximations, we tested the colors produced for the modern Earth sky and Titan as a check, and the results appeared reasonable. Colors and photometric bands have been considered as indicators of Earth-like worlds (Traub, 2003; Crow *et al.*, 2011; Krissansen-Totton *et al.*, 2016), but hazy Archean Earth suggests that not all Earth-like planets will be pale blue dots. Because methane-producing metabolisms evolved early and Earth's atmosphere was anoxic for about a billion years after the origin of life, pale orange dots may proliferate in the Galaxy if other habitable worlds evolve on similar paths to Earth.

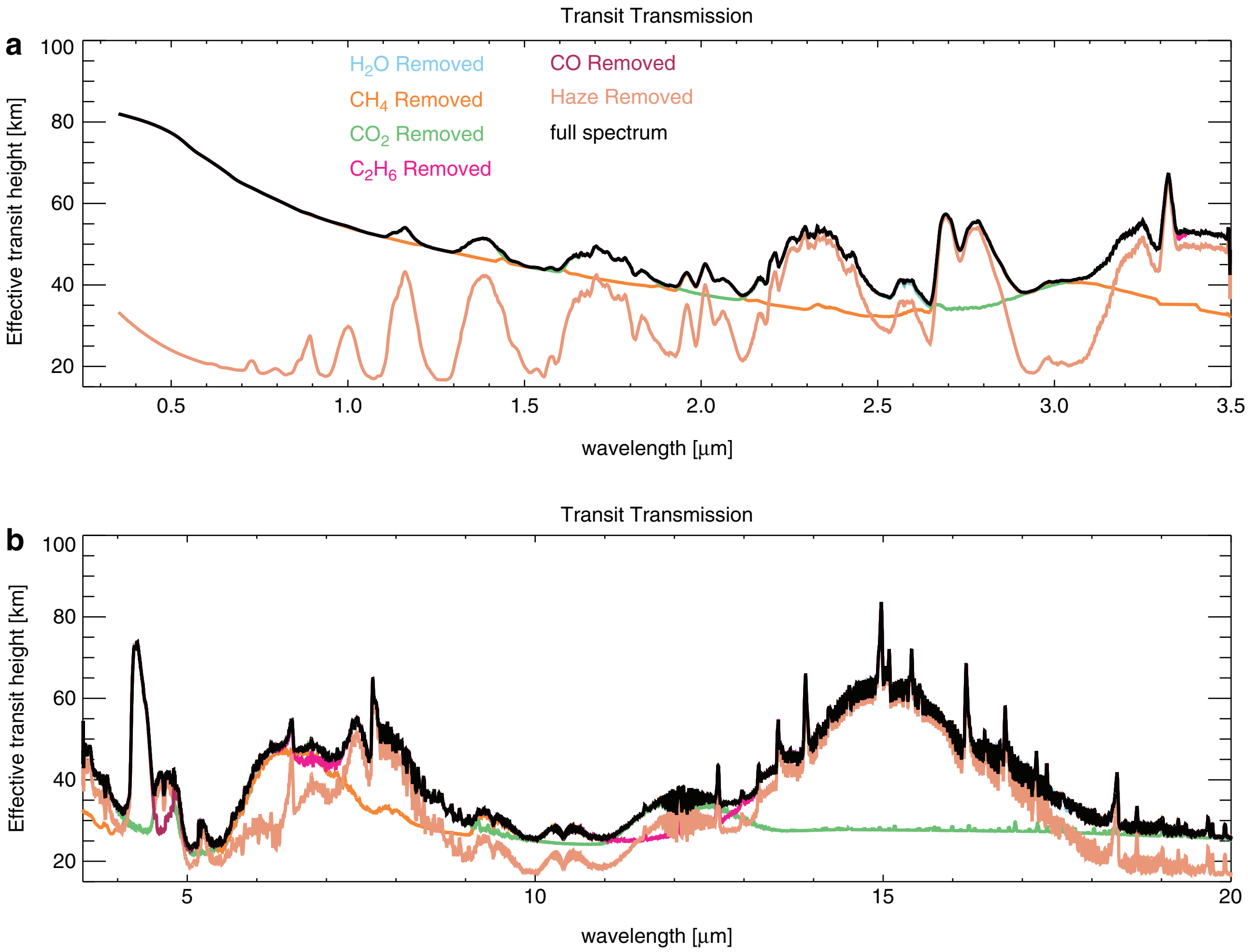

**FIG. 10.** A transit transmission spectrum for a hazy Case B planet in the visible and NIR (**a**) and mid-IR (**b**) is presented with gases and the hydrocarbon haze removed to show where each spectral component interacts with radiation. The full spectrum is shown in black. Places where the black spectrum deviates from the colored spectra indicate where each gas or haze absorbs. For example, the orange line in (A) indicates $CH_4$ absorption features near 1.15, 1.4, 1.7, 2.3, and 3.3 $\mu$m.

Several spectral features are apparent in Fig. 8. The haze-mediated stratospheric thermal inversion is clearly seen in thermal emission near 8 and 16 $\mu$m (Fig. 8b). Similar to the Titan transmission spectrum derived from Cassini solar occultation measurements (Robinson *et al.*, 2014b), our simulated hazy transit transmission spectra (Fig. 8c) are sloped in the visible and NIR. Gas absorption features in the visible and NIR are muted by the presence of a haze in transit transmission, but mid-IR absorption features are less affected because the haze is relatively transparent at longer wavelengths. In Earth-like clear-sky atmospheres, the minimum atmospheric altitude transit observations are able to probe will typically be limited by refraction (García Muñoz *et al.*, 2012; Bétrémieux and Kaltenegger, 2014; Misra *et al.*, 2014b), but in hazy atmospheres, haze controls the minimum effective tangent height, especially at shorter wavelengths where it controls the transit transmission spectral slope. Absorption from the haze itself can be seen as the ‘‘bump’’ in the ‘‘thick’’ haze ($CH_4/CO_2 = 0.21$) transit transmission spectrum at 6 $\mu$m, a wavelength region accessible with the James Webb Space Telescope (Wright *et al.*, 2004). There is also a very weak haze feature near 3 $\mu$m in transit transmission that can be most easily seen in Fig. 10. These features can also be seen in the peaks of the haze imaginary refractive index (Fig. 2).

Note the presence of a $C_2H_6$ absorption feature near 12 $\mu$m. This $C_2H_6$ forms from photochemistry involving $CH_4$, and its buildup in our spectra is not inconsistent with the results of Domagal-Goldman *et al.* (2011), which showed much greater $C_2H_6$ accumulation on planets orbiting low-mass stars compared to worlds orbiting the Sun. However, the $CH_4$ levels in the Domagal-Goldman *et al.* solar simulations were an order of magnitude lower than the ones shown here. $C_2H_6$ is a greenhouse gas, and its ability to warm in a $CH_4$- and haze-rich atmosphere has been discussed previously (Haqq-Misra *et al.*, 2008).

Figures 8–10 showed spectra for our Case B planet, but Figs. 11 and 12 show representative reflected light and transit transmission spectra for all our Cases A–D in the visible and NIR. The reflectance spectra in Figs. 8 and 9 assumed a pure ocean surface albedo to isolate the spectral consequence of atmospheric haze from other spectral

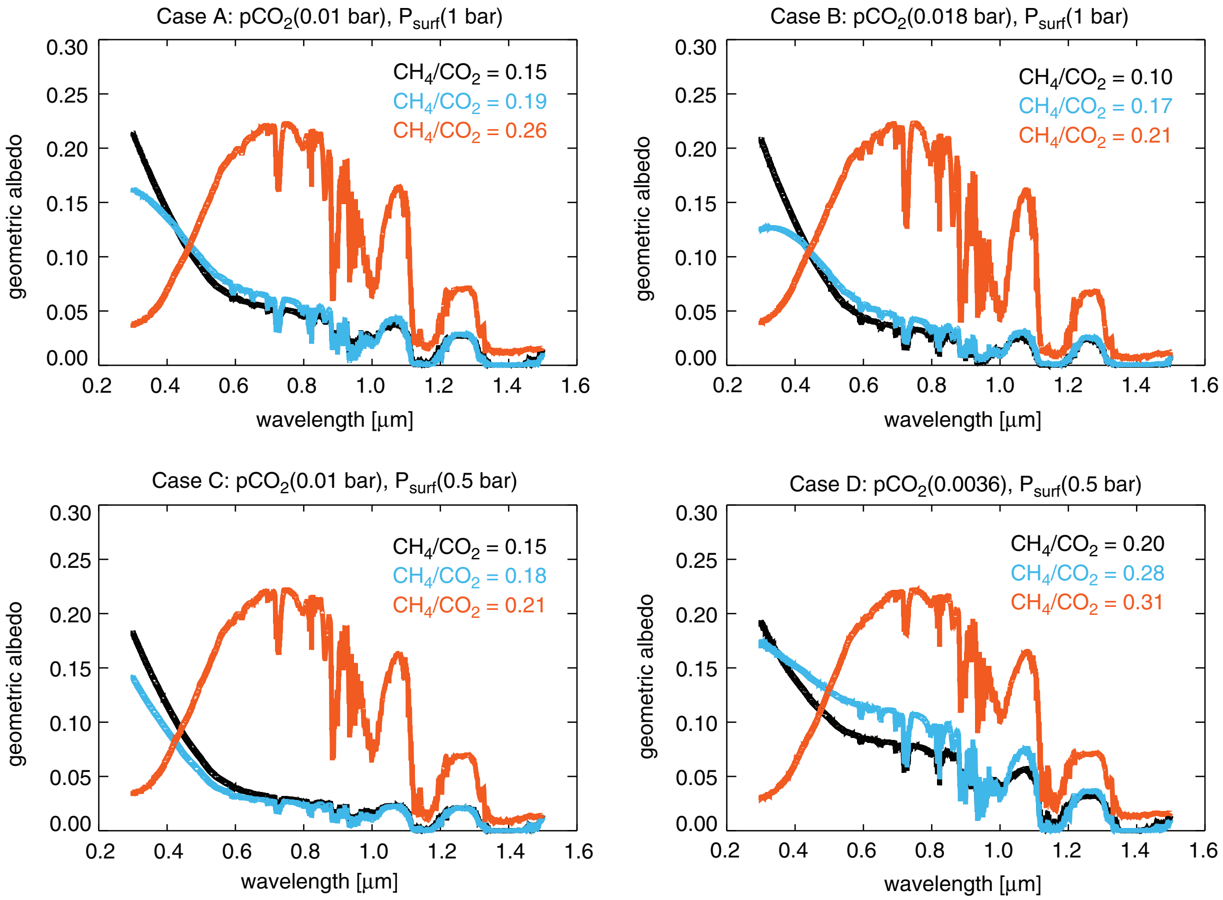

**FIG. 11.** Example reflectance spectra, intended as analogues for exoplanets like Archean Earth, for all the types of planets investigated in this study are presented here. Fractional ice coverage is included in these spectra using a weighted average of icy and liquid water surfaces as described in the text.

changes, but the spectra shown in Fig. 11 are constructed from a weighted average of ocean and ice surfaces according to the ice line latitudes reported by Wolf and Toon (2013) for Archean atmospheres with $CO_2$ and $CH_4$. The hazy planets in Fig. 11 are more reflective than the spectra shown in Fig. 8 due to this ice coverage. Figure 12 shows how thick hazes strongly mute the strength of gaseous absorption features in transit transmission at shorter wavelengths where these hazes are more optically thick.

**3.3.1. Water clouds.** The goal of the nominal haze spectra we have presented is to show the spectral impact of organic haze independent of any other atmospheric aerosols. However, it is interesting and important to also consider how water clouds affect our hazy spectra. To test the impact of clouds in addition to haze on the spectra of Earth-like planets, we added water clouds to the Case B atmospheres shown in Fig. 8. Because these are 1-D spectra, we incorporate clouds with a weighted average of cloudy and pure haze spectra where we assume 50% of the planet is covered by haze only, 25% is covered by cirrus clouds (at 10 km altitude) and haze, and 25% by stratocumulus clouds (at 1 km altitude) and haze (Robinson *et al.*, 2011). The resulting spectra are presented in Fig. 13. In contrast to hydrocarbon haze particles, which are more transparent in the NIR compared to shorter wavelengths, water vapor clouds have an approximately gray opacity from the visible into the NIR. Thus, at longer wavelengths, cloudy worlds are brighter than their haze-only counterparts. Table 4 shows the total integrated brightness of the reflectance spectra for the worlds with clouds divided by their cloud-free counterparts between 0.4 and 1 $\mu$m and between 1 and 2 $\mu$m to quantify the spectral impact of clouds.

The disproportionate increase in brightness from clouds at longer wavelength compared to shorter wavelengths means that the peak of the reflectance spectrum also shifts toward longer wavelengths for the worlds with clouds: for $CH_4/CO_2 = 0.17$, the reflectance spectrum peak shifts from 0.31 to 0.38 $\mu$m, and for $CH_4/CO_2 = 0.21$, it shifts from 0.56 to 0.68 $\mu$m. Adding clouds also raises the spectral continuum level, making absorption features appear deeper. This enhanced reflectivity also potentially increases the detectability of water vapor in reflected light spectra, as more reflected flux from the planet reduces noise on the continuum, enhancing the detectability of absorption features that deviate from that continuum. A detailed discussion of the impact of water clouds on the spectra of Earth-like planets for different cloud altitudes and fractional cloud coverages can be found in the work of Kitzmann *et al.* (2011b).

In transit transmission, water clouds have no spectral impact because they form in the atmosphere at a level below the maximum tangent height set by refraction. The

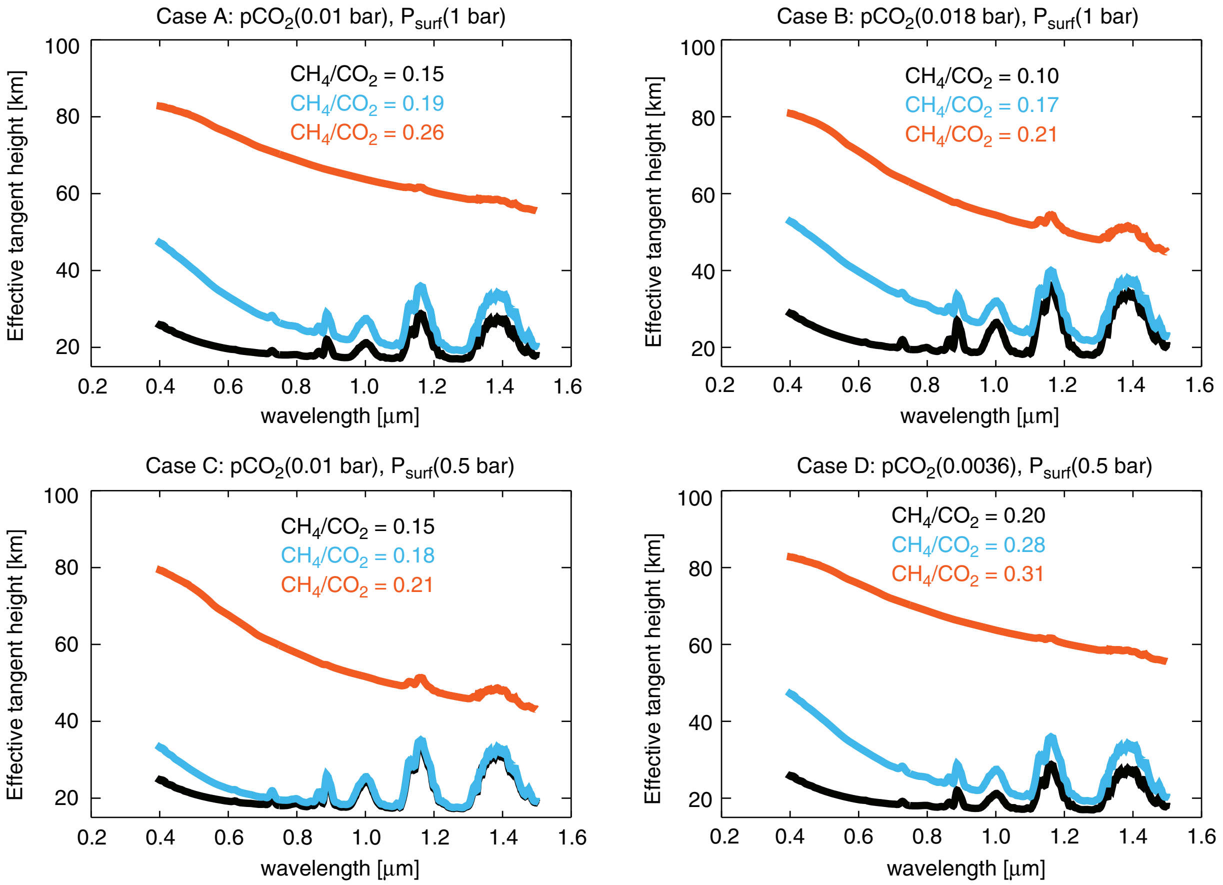

**FIG. 12.** Transit transmission spectra in the visible and NIR for Cases A–D are presented here. For thicker hazes, absorption features shortward of approximately 1 $\mu$m vanish. These relatively featureless spectra result because high-altitude hazes are effective at obscuring the lower atmosphere with the long path lengths taken by light in transit spectroscopy measurements.

tropopause on Earth is at roughly 10 km, and refraction prohibits transmission of path lengths below about 20 km even for our clear-sky worlds. As water vapor is at very low abundance in Earth's stratosphere, it would be difficult, in general, to see it in transmission observations that can only probe down to stratospheric altitudes. Abundant stratospheric water vapor would imply that the planet is in the midst of a moist or runaway greenhouse state and thus is not conventionally habitable.

## 4. Discussion

The hazes investigated here have a major spectral impact at short wavelengths due to their strong blue and UV absorption. It has been suggested that the Rayleigh scattering slope could be used to constrain atmospheric pressure on exoplanets (Benneke and Seager, 2012), but this would not be possible on planets with hydrocarbon hazes due to these strong short-wavelength absorption effects. In reflected light, the haze's broadband UV absorption feature, observed together with methane bands, would strongly imply the existence of hydrocarbon haze in an atmosphere. In the IR, the diagnostic haze absorption feature at 6 $\mu$m (and the weaker one at 3 $\mu$m) in transit transmission would allow chemical identification of hydrocarbon haze. Even absent the detection of these specific features in transit transmission, the presence of $CH_4$ bands together with the haze UV-visible-NIR spectral slope would strongly imply the presence of this haze.

### *4.1. Haze and biology*

Our study shows how an Archean haze would have profoundly impacted our planet's environment, habitability, and spectrum. It is important to note that geochemical evidence suggests hazy conditions were not present throughout the entire Archean, and its periodic collapse may have put stress on the biosphere if organisms migrated to the surface or near-surface and adapted to lower UV levels created by the haze. On the other hand, if organisms remained protected by some other UV shield such as minerals, layers of overlying microbial mat, or water (Cockell, 1998), changes in UV radiation levels should not affect them as strongly, so the colder conditions created by the haze might have been the larger source of stress on organisms. These stressors might have driven evolutionary adaptations as life responded to its changing environment. Note that photosynthetic organisms would not likely have been photon limited by the lower light levels under the haze: the lower light limit for red algae is $6 \times 10^{15}$ photons/m$^2$/s (Littler *et al.*, 1986). Under our Case B $CH_4/CO_2 = 0.21$ haze, total PAR at the surface is $7.1 \times 10^{20}$ photons/m$^2$/s, orders of magnitude above this extreme.

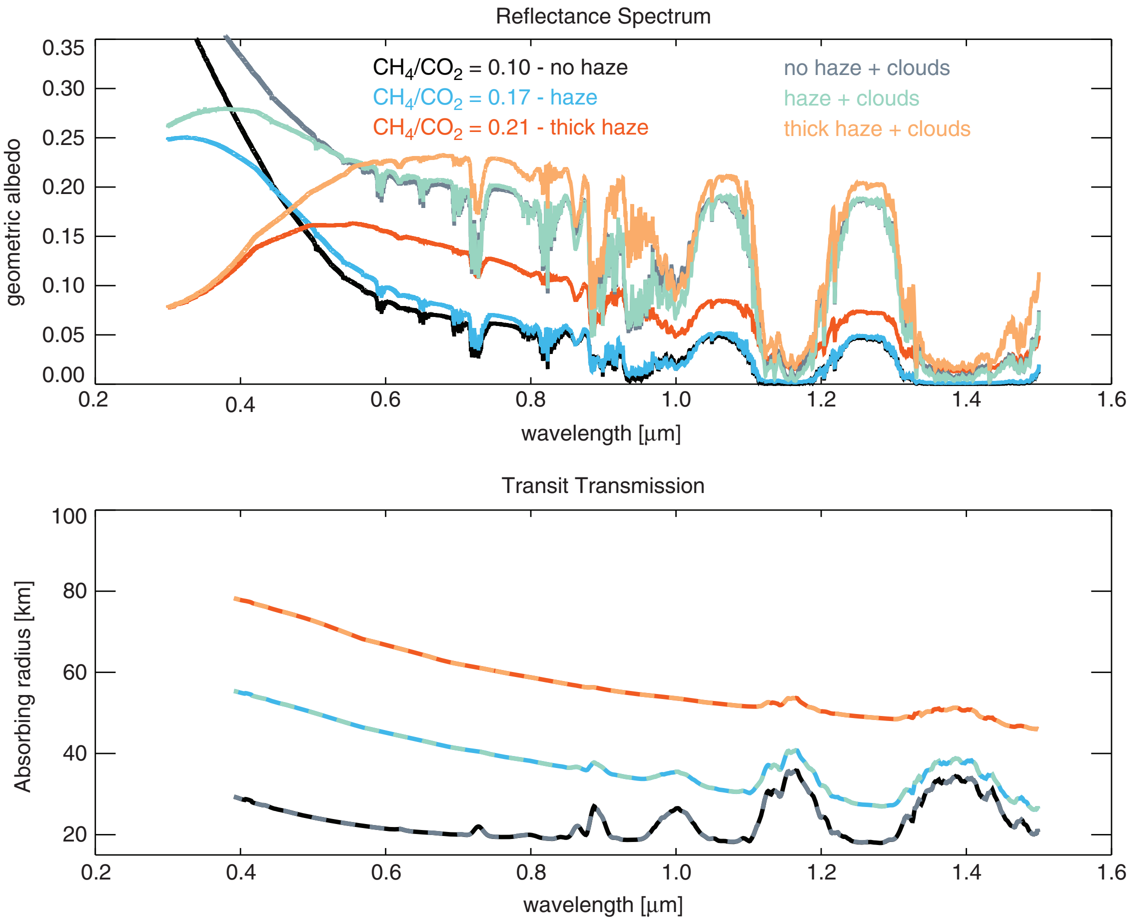

**FIG. 13.** Here we show the impact of water clouds on our Case B spectra with no haze, a thin haze, and a thick haze. The spectra with cloud and haze are shown in the pale colored lines. The dashed lines over our transit transmission spectra indicate that the spectra with and without water clouds are the same.

Laboratory experiments on organic haze formation have shown that haze-formation chemistry can involve the formation of important prebiotic molecules such as amino acids and nucleotide bases (Khare *et al.*, 1986; McDonald *et al.*, 1994; DeWitt *et al.*, 2009; Hörst *et al.*, 2012; Trainer, 2013)—see also our discussion of haze formation pathways in Section 4.4. Although the hazy periods we invoke here occurred hundreds of millions of years after the origin of life on Earth, there may be earlier hazy epochs not yet discovered in the geological record [see Kasting (2005) for a discussion of earlier atmospheric methane], and hazy Titan has been regarded as a type of prebiotic chemical laboratory (Khare *et al.*, 1984b; Clarke and Ferris, 1997).

TABLE 4. THE RELATIVE BRIGHTNESS OF SPECTRA WITH AND WITHOUT WATER CLOUDS

| *$CH_4/CO_2$ =* | *0.4–1 μm With clouds/ No clouds* | *1–2 μm With clouds/ No clouds* |
|---|---|---|
| 0.10 | 2.34 | 4.80 |
| 0.17 | 2.12 | 4.24 |
| 0.21 | 1.56 | 2.24 |

While we know that abiotic hydrocarbon hazes are possible (*e.g.*, on extremely cold worlds like Titan with reducing atmospheres), on a planet like Archean Earth, the presence of hydrocarbon haze may require a higher level of methane production than is possible from abiotic sources alone. The maximum abiotic methane production rate from serpentinization, its primary nonbiological source, has been estimated as $6.8\times10^8$ and $1.3\times10^9$ molecules/cm$^2$/s for rocky planets of 1 and 5 Earth masses, respectively (Guzmán-Marmolejo *et al.*, 2013), although there has been earlier speculation of higher abiotic production rates (Kasting, 2005; Shaw, 2008), especially if ancient seafloor spreading rates were faster or the amount of iron-rich ancient seafloor rock was greater. Based on their calculations, Guzmán-Marmolejo *et al.* (2013) suggested that an atmospheric $CH_4$ concentration greater than 10 ppmv is suggestive of life. At the range of $pCO_2$ allowed by Driese *et al.* (2011), we find that the $CH_4$ flux needed to initiate haze formation ranges between about $1\times10^{11}$ and $3\times10^{11}$ molecules/cm$^2$/s, broadly consistent with estimates for the biological Archean methane flux after the origin of oxygenic photosynthesis (Kharecha *et al.*, 2005; Claire *et al.*, 2014). The higher of the plausible rocky planet abiotic $CH_4$ fluxes from Guzmán-Marmolejo *et al.*, $1.3\times10^9$ molecules/cm$^2$/s, will not form a haze in our model even at a $pCO_2$ level 4 orders of magnitude smaller than the lower limit allowed by Driese *et al.* (2011), and such a world would be completely frozen given the Archean solar constant. Remote identification of a hydrocarbon haze with a concurrent measurement of $CO_2$ around a planet that absorbs an Earth-like amount of radiation could therefore imply a surface methane flux consistent with biological production. The strength and width of the hydrocarbon haze absorption feature below about 0.5 $\mu$m implies it would be easier to detect than methane itself given sufficient instrumental sensitivity to this range, so the occurrence of haze in the habitable zone may be a way to flag interesting planets for careful follow-up study that would search for other indicators of life and quantify the concentration of $CH_4$ and other gases.

### 4.2. Comparison with other climate studies

To test the robustness of the mean surface temperatures calculated by our computationally efficient 1-D climate model, we compared our temperature result for a haze-free Case A atmosphere with $pCO_2 = 0.01$ and $pCH_4 = 0.002$ (but no ethane) and a solar constant for 2.5 billion years ago to the Laboratoire de Météorologie Dynamique (LMD) GCM run with the same inputs. We adopt the same average albedo produced by the LMD model in this simulation, setting $A_{surf} = 0.33$ for our planet (as before, this albedo includes the effect of clouds). For an ocean-covered planet with no haze, the LMD model produces a mean surface temperature of 287 K (Charnay *et al.*, 2013). This is comparable to, but 5 K warmer than, our global average 1-D result of 282 K. The Charnay *et al.* results for the same atmospheric properties but with an equatorial supercontinent result in the same overall planetary albedo (0.33) but a lower mean temperature of 285 K, which is closer to our result. We achieve the closest match to the Charnay *et al.* results for a modern continental land mass arrangement: in the GCM, this yields an average albedo of 0.34 and a temperature of 283.7 K, close to our result of 281.1 K for this configuration.

We also tested our model results against the Community Atmosphere Model (CAM) GCM nominal Archean atmosphere reported by Wolf and Toon (2013). For this planet, the solar constant is 80% modern, $pCO_2 = 0.06$ bar, there is no $CH_4$, no haze, and the planet has an average albedo of 0.317. For this world, the CAM produces a global average surface temperature of 287.9 K. Our model produces 285.3 K for this configuration, a difference of 2.6 K.

The GCMs we compare to can include a variety of effects our 1-D model cannot, including atmospheric circulation, precipitation, cloud formation, and cloud scattering and absorption. Our comparison with these 3-D models suggests the temperatures we present in this work are reasonable but may be underestimates by about 3–5 K. One reason that our 1-D results may be colder than the GCM results is that while we have incorporated identical planetary albedos (with clouds), we are still missing the long-wave radiative forcing from clouds, which would have a warming effect.

Haqq-Misra *et al.* (2008) similarly studied the climate of Archean Earth with hydrocarbon hazes and high amounts of $CO_2$, $CH_4$, and $C_2H_6$ with an earlier incarnation of the 1-D models we use here. The haze-free surface temperatures we generate are broadly consistent with the Haqq-Misra *et al.* nonhazy results with $C_2H_6$. Haqq-Misra *et al.* show that a planet with $pCO_2 = 0.01$ and $CH_4/CO_2 = 0.1$ has a surface temperature of about 282 K, which is close to our 283.4 K for a comparable atmosphere. Similar to our study, the Haqq-Misra *et al.* study found it was difficult to maintain surface temperatures above the freezing point of water with spherical haze particles. However, as we have argued, a mean surface temperature of the freezing point of water is not a useful threshold for global habitability (Charnay *et al.*, 2013; Shields *et al.*, 2013; Wolf and Toon, 2013; Kunze *et al.*, 2014), so some of the Haqq-Misra *et al.* spherical haze results may actually be ''habitable.'' In general, we are able to achieve warmer hazy solutions in our study because, as previously discussed, fractal hydrocarbon hazes produce less extinction of visible wavelengths compared to equal-mass spherical haze particles. For example, for a planet with 1 bar of pressure and 2% $CO_2$, the Haqq-Misra *et al.* spherical haze drops the planet's temperature to below 260 K. The same planet with a fractal haze in our study remains above 273 K (without considering ice-albedo effects not examined by the Haqq-Misra *et al.* study) after haze self-shielding levels off the temperature. Our results suggest that fractal hazes do indeed produce less antigreenhouse cooling than spherical particles. However, since our nonhazy comparison atmosphere was about 1.4 K warmer than the comparable Haqq-Misra atmosphere, a small component of the warmer temperatures we see here may also result in part from updates to our climate model made by Kopparapu *et al.* (2013).

### 4.3. Potential for $NH_3$ greenhouse gas shielding

The optical thickness of the haze impacts its ability to shield molecules from photodissociation. Once the UV opacity of the haze exceeds approximately unity, the surface flux of $CH_4$ necessary to maintain a given atmospheric methane mixing ratio drops due to haze-induced $CH_4$ shielding. At higher haze thicknesses, the opacity of the haze levels off because this self-shielding inhibits the methane photolysis needed to initiate haze formation. Wolf and Toon (2010) commented on the possibility of a fractal hydrocarbon haze shielding ammonia ($NH_3$) from photolysis, allowing this greenhouse gas to build up in the Archean atmosphere. Following Sagan and Chyba (1997), Wolf and Toon calculated a $NH_3$ atmospheric lifetime of $7 \times 10^7$ years for a solar incident flux at a 45° angle assuming $\tau \sim 11$ at 200 nm. Following Wolf and Toon, we find our maximum haze thickness levels off at $\tau \sim 5$ at 200 nm, which results in a significantly shorter $NH_3$ lifetime of $1 \times 10^4$ years, although we did not include $NH_3$ in our photochemical scheme. Our future work will include $NH_3$ in the photochemical and climate model to study, in a self-consistent atmosphere, how much of this gas can exist in a hazy atmosphere and what its climatic effect could be.

### 4.4. Haze formation pathways

Following the mechanism proposed for the formation of Titan's hydrocarbon haze (Allen *et al.*, 1980; Yung *et al.*, 1984), every model of hydrocarbon haze formation in early Earth's atmosphere—including ours—has assumed that aerosol formation will occur through the formation of acetylene ($C_2H_2$) and its further polymerization to higher polyacetylene chains (Pavlov *et al.*, 2001b; Domagal-Goldman *et al.*, 2008; Haqq-Misra *et al.*, 2008; Zerkle *et al.*, 2012;

Kurzweil *et al.*, 2013; Claire *et al.*, 2014). The two reaction pathways described in Section 2.1.1 provide an initial picture of the process, but haze formation is likely considerably more complex and is still not well understood. Unlike early Earth, we now have access to direct observations of the chemical processes ongoing in Titan's atmosphere. *In situ* measurements by several instruments on board Cassini have found direct evidence for long hydrocarbons and nitriles chains, benzene ($C_6H_6$) and toluene ($C_6H_5CH_3$), and indirect evidence for polycyclic aromatic hydrocarbons (PAHs) and nitrogen-containing polycyclic aromatic hydrocarbons (PANHs), indicating that these compounds might play a role in the formation of Titan's hazes (Waite *et al.*, 2007; López-Puertas *et al.*, 2013).

Moreover, early Earth's atmosphere was likely not as reducing as Titan's. The chemical pathways for haze formation, including the $C_2H_2$ polymerization pathways, may therefore be inappropriate. Early Earth's atmosphere would have contained negligible $O_2$ but significant amounts of $CO_2$ (*e.g.*, Kasting, 1993; Driese *et al.*, 2011), whereas Titan's atmosphere is extremely reducing (de Kok *et al.*, 2007). Even in Titan's highly reducing atmosphere, it was suggested that CO may contribute to oxygen incorporation in the organic aerosols (Hörst *et al.*, 2012). This oxygen incorporation is expected to be much more important to aerosol chemistry in early Earth's far less reducing atmosphere. By using far-UV radiation (115–400 nm), organic aerosol production from a $CH_4/CO_2/N_2$ mixture was shown to exceed that from a pure $CH_4/N_2$ mixture (Trainer *et al.*, 2006), and organic aerosol formation was experimentally observed to occur down to C/O ratios as low as 0.1 (Trainer *et al.*, 2006; DeWitt *et al.*, 2009). From the chemical analysis of primary condensed-phase products of photochemistry, it is clear that the composition of the aerosol analogues formed in early Earth-like atmospheres with $C/O < 1$ differs greatly from the aerosol analogues formed in Titan-like atmospheres where $C/O >> 1$. Instead of limiting the formation of organic molecules as initially predicted, the O-atoms released from $CO_2$ photolysis are incorporated into the molecular structure of the organic aerosols. Mass spectrometry of aerosol analogues formed with $C/O = 0.1$ indicates the formation of carbonyl and carboxyl groups rather than aromatic cycles and long-aliphatic chains, and even suggests the formation of organic acids such as succinic acid ($C_4H_6O_4$) (DeWitt *et al.*, 2009).

Finally, haze formation chemistry gets considerably more complex when one considers the coexistence not only of O-heteroatoms but also of N-heteroatoms in aerosol organics. Nitrogen incorporation was recently observed in the aerosols generated by far-UV photolysis of $CH_4/CO_2/N_2$ gas mixtures (Trainer, 2013) and in $CH_4/N_2$ mixtures (Sebree *et al.*, 2015). These results bring to light a significant but still unknown mechanism regarding the activation of nitrogen and its inclusion in oxygenated organics, thus providing a new and quantifiable source for these two elements into the early Earth aerosols. Studies have shown the formation of HCN, $CH_3CN$, and other nitrile gas species are formed using the same type of UV source in a $CH_4/N_2$ gas mixture, thus corroborating the indirect nitrogen photochemistry (Trainer *et al.*, 2012; Yoon *et al.*, 2014). These results suggest that $N_2$ chemical activation could be due to its reaction with the methylidyne (CH) radical formed from $CH_4$ photolysis, to form two radical intermediates, diazomethyl HCNN and its isomer HNCN, which might then react to form HCN and other products.

The formation of aerosols in early Earth's atmosphere is thus tightly intertwined with the formation of organic molecules containing more than a few C/H/N/O atoms. These compositional differences should change the properties of the aerosol material sufficiently to be able to distinguish a hazy early Earth from a modern-day Titan (Hasenkopf *et al.*, 2010). For instance, organic molecules with oxygen-containing functional groups (alcohols, carbonyls) tend to have stronger absorbances at longer UV wavelengths as compared to similar hydrocarbon molecules (Workman, 2000). The NIR absorption bands of the Archean aerosol

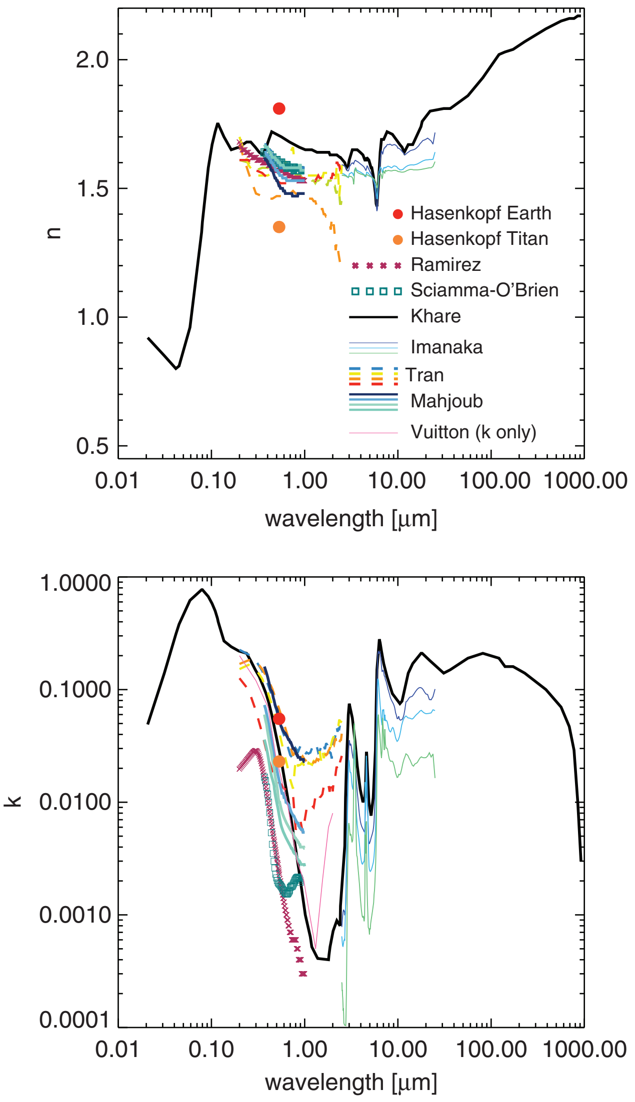

**FIG. 14.** This shows the diversity of optical constants measured by several studies. The studies the figure key refers to are as follows: Hasenkopf *et al.*, 2010; Ramirez *et al.*, 2002; Sciamma-O'Brien *et al.*, 2012; Khare *et al.*, 1984a; Imanaka *et al.*, 2012; Tran *et al.*, 2003; Mahjoub *et al.*, 2012; Vuitton *et al.*, 2009. Note in particular the single point measured under Archean Earth-like laboratory conditions by Hasenkopf *et al.* (2010).

analogues would also shift in response to the inclusion of the types of oxygen and nitrogen heteroatom functionalities that have been indicated in the compositional studies.

### *4.5. Optical constants*

The implications of compositional differences of Archean hazes versus titanian hazes for the topics presented in this study and for prebiotic chemistry underscore the need for measurements of Archean Earth analog optical constants as well as a better understanding of the haze formation chemical pathways. Unfortunately, only one study, that of Hasenkopf *et al.* (2010), has measured an Archean Earth haze refractive index (as opposed to a titanian haze), and this was only done at a single wavelength (532 nm).

In our study, we have used the hydrocarbon refractive indices from the work of Khare *et al.* (1984a) to allow us to draw comparisons with previous works involving our suite of models (Pavlov *et al.*, 2001b; Domagal-Goldman *et al.*, 2008; Haqq-Misra *et al.*, 2008; Zerkle *et al.*, 2012; Kurzweil *et al.*, 2013; Claire *et al.*, 2014), as well as the Wolf and Toon (2010) study, which all used the Khare optical constants. An additional advantage of the Khare refractive indices is that they span an extremely wide wavelength range, ranging from 0.02 to 920 $\mu$m, so only one set of optical constants is needed to cover all the wavelengths relevant to photochemistry, climate, and spectra.

However, more recent measurements of hydrocarbon refractive indices over more restricted wavelength ranges indicate disagreement with the Khare measurements (Ramirez *et al.*, 2002; Tran *et al.*, 2003; Vuitton *et al.*, 2009; Hasenkopf *et al.*, 2010; Imanaka *et al.*, 2012; Mahjoub *et al.*, 2012; Sciamma-O'Brien *et al.*, 2012), although these measurements themselves show considerable variation among each other (Fig. 14). Differences in the composition of Archean hazes compared to Titan's (and thus differences in their optical constants) are expected as discussed in Section 4.4. Again, note the single measurement by Hasenkopf *et al.* (2010) for an Archean analog haze; of all the optical constants plotted in Fig. 14, the Khare indices actually produce the closest (although still too low) match to the Hasenkopf Archean real refractive index ($n$) near 532 nm and produce a reasonable match to the Hasenkopf Archean imaginary refractive index ($k$), agreeing to within approximately 40% near 532 nm.

As an example and test of the impact different refractive indices have on our spectra, we examined the sensitivity of our nominal spectra to varied refractive indices measured by Mahjoub *et al.* (2012). The Mahjoub study tested the impact of methane concentration in the gas phase on the resultant hydrocarbon optical properties with gas mixtures containing 1%, 2%, 5%, and 10% $CH_4$ in $CH_4$-$N_2$ mixtures. Note the 1% $CH_4$ Mahjoub imaginary refractive index agrees to within 5% of the Hasenkopf Archean measurement near 532 nm. Mahjoub *et al.* found that refractive indices have a strong dependency on the $CH_4$ concentration over 0.37–1 $\mu$m: results indicate that the imaginary index of refraction ($k$) decreases with increasing $CH_4$ concentration, and the real index of refraction ($n$) increases with $CH_4$ for the compositions tested. We generated the spectra shown in Fig. 15 by producing new fractal input files using the Mahjoub optical constants. These files were then used to replace the Khare files in our SMART inputs for the nominal $CH_4/CO_2 = 0.21$ Case B spectrum. In addition, we generated a spectrum to test the Hasenkopf Archean haze measurement by applying a scaling factor to the Khare optical constants to match the Hasenkopf $n$ and $k$ values at 532 nm. This spectrum is called ''Khare-Hasenkopf'' in the Fig. 15 caption. Of course this does not account for differences expected in the spectral shape of Archean haze analogues across the UV-visible-IR relative to the titanian haze analogues.

Besides affecting the top-of-atmosphere spectrum, these different optical constants alter how much radiation can reach the surface under a haze. We find that, for the

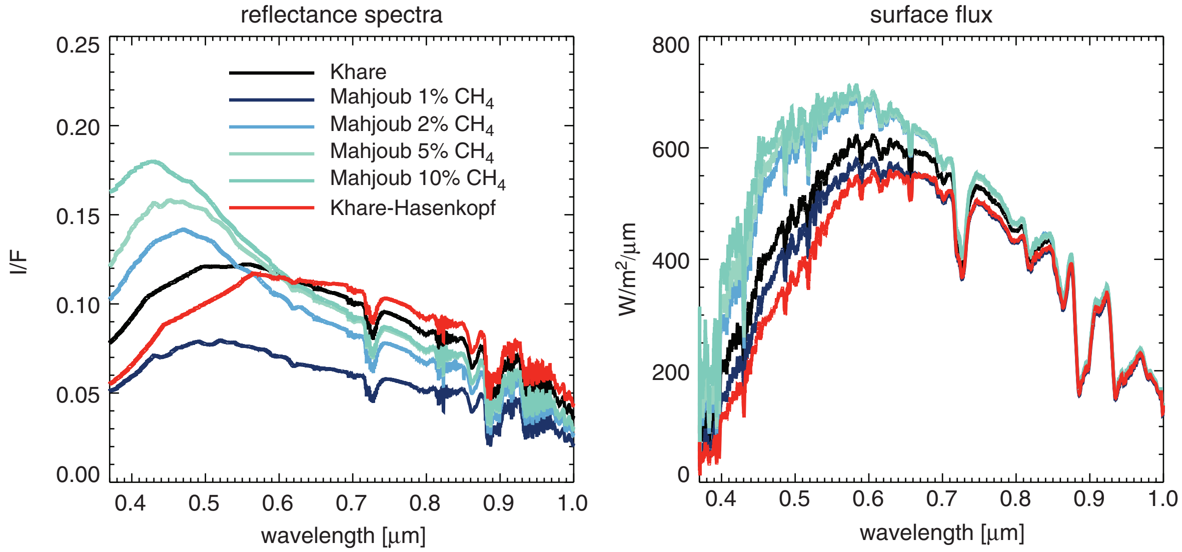

**FIG. 15.** A comparison of reflectance spectra and surface flux spectra using Khare *et al.* (1984a) and Mahjoub *et al.* (2012) optical constants, plus a spectrum generated by shifting the Khare constants to match the Archean haze refractive indices measured by Hasenkopf *et al.* (2010) at 532 nm (called ''Khare-Hasenkopf'').

Mahjoub 1%, 2%, 5%, and 10% $CH_4$ optical constants, 0.92, 1.11, 1.13, and 1.16 times the nominal (Khare) total integrated 0.37–1 $\mu$m flux reaches the surface of the planet. For the Khare-Hasenkopf spectrum, which shifts both the real and imaginary refractive indices to larger values, this drops to 0.89 times the nominal flux. The Mahjoub constants do not extend shortward of 0.37 $\mu$m, but we should anticipate variation at these shorter wavelengths as well.

The variation in surface-incident flux shows us that we should expect differences in the hazy Archean climates we calculate depending on the optical constants used. We tested how the Hasenkopf Archean measurement might impact the climate for a $pCO_2 = 0.01$ and $CH_4/CO_2 = 0.2$ atmosphere. The nominal Khare constants produce a surface temperature of 272 K for this atmosphere. The ''Khare-Hasenkopf'' optical constants yield a cooler temperature of 267 K, which is expected because these optical constants produce a haze with more efficient scattering and absorption. This difference in temperature is smaller than the difference of using spherical versus fractal particles: our comparison to the Haqq-Misra *et al.* (2008) study in Section 4.2 shows that particle shape can result in temperature differences >10 K. A full treatment of the impact of varied optical constants using the coupled photochemical-climate model to generate new self-consistent atmospheres and climates is outside the scope of our present study.

Updated haze optical constants generated under Archean Earth-like laboratory conditions (rather than Titan-like conditions) to produce plausible Archean analog haze compositions would be of immense value to future studies of organic hazes in Earth-like atmospheres, including exoplanets, and would allow updates of the results presented in this study. Due to the properties of fractal hazes, these particles are relatively transparent at wavelengths longer than approximately the visible range, so measurements of refractive indices at visible wavelengths in particular would allow us to improve our estimates of the climatic impacts of this haze. In addition, better constraints on Archean UV refractive indices would allow us to better quantify how good a UV shield these hazes actually are.

## 5. Conclusions

We have shown that a hazy Archean Earth consistent with geochemical constraints on $CO_2$ concentration and geological constraints on surface pressure could have had habitable surface temperatures. Although the fractal hazes simulated here cool the planet by up to $\sim 20$ K, these fractal particles produce significantly less cooling than a haze of equivalent-mass spherical particles. The climatic effects of this haze could have been part of feedbacks between biological $CH_4$ production, atmospheric chemistry, and surface UV radiation. Haze can cut down the surface-incident UVC radiation on Archean Earth from $\sim 0.9\ W/m^2$ to $\sim 0.03\ W/m^2$ for a SZA of 60°, and may have allowed survival of otherwise unshielded life at the surface of our Archean planet. The presence of similar hydrocarbon haze on an exoplanet could be observed, as demonstrated by strong features present in synthetic spectra of these worlds. For habitable exoplanets similar to Archean Earth, hydrocarbon haze may be strongly biologically mediated and serve as a novel non-gaseous biosignature with a strong spectral signature. Discovering habitable exoplanets dissimilar to modern Earth will increase the diversity of known habitable environments. Leveraging our understanding of Earth's history provides us with a variety of analogues with which we can expand our expectations for the ''Earth-like'' planets beyond our solar system; future observations of such worlds can provide us with a window into the evolution of terrestrial worlds like our home.

## Acknowledgments

This work was performed as part of the NASA Astrobiology Institute's Virtual Planetary Laboratory, supported by the National Aeronautics and Space Administration through the NASA Astrobiology Institute under solicitation NNH12ZDA002C and Cooperative Agreement Number NNA13AA93A. G. Arney was supported in part by the NASA Astrobiology Institute Early Career Collaboration Award. E.T. Wolf acknowledges NASA Planetary Atmospheres Program award NNH13ZDA001N-PATM and NASA Exobiology Program award NNX10AR17G for financial support. B. Charnay acknowledges support from an appointment to the NASA Postdoctoral Program, administered by Universities Space Research Association. E. Hébrard was supported by an appointment to the NASA Postdoctoral Program at NASA Goddard Space Flight Center, administered by Universities Space Research Association through a contract with NASA. Simulations were facilitated through the use of the Hyak supercomputer system at the University of Washington eScience Institute. We are grateful to C. McKay and three other anonymous reviewers whose comments substantially improved the quality of our manuscript. We thank R. Buick, D. Crisp, N. Kiang, and M. Parenteau for conversations and advice. Spectra shown in this work will be archived at the Virtual Planetary Laboratory online spectral database.

## Author Disclosure Statement

No competing financial interests exist.

## References

Abbot, D.S., Voigt, A., and Koll, D. (2011) The Jormungand global climate state and implications for Neoproterozoic glaciations. *J Geophys Res* 116, doi:10.1029/2011JD015927.

Allen, M., Pinto, J.P., and Yung, Y.L. (1980) Titan: aerosol photochemistry and variations related to the sunspot cycle. *Astrophys J* 242:L125–L128.

Allwood, A.C., Walter, M.R., Kamber, B.S., Marshall, C.P., and Burch, I.W. (2006) Stromatolite reef from the Early Archaean era of Australia. *Nature* 441:714–718.

Arney, G., Meadows, V., Crisp, D., Schmidt, S.J., Bailey, J., and Robinson, T. (2014) Spatially resolved measurements of $H_2O$, HCl, CO, OCS, $SO_2$, cloud opacity, and acid concentration in the Venus near-infrared spectral windows. *J Geophys Res: Planets* 119:1860–1891.

Bardeen, C.G., Toon, O.B., Jensen, E.J., Marsh, D.R., and Harvey, V.L. (2008) Numerical simulations of the three-dimensional distribution of meteoric dust in the mesosphere and upper stratosphere. *J Geophys Res: Atmospheres* 113, doi:10.1029/2007JD009515.

Benneke, B. and Seager, S. (2012) Atmospheric retrieval for super-Earths: uniquely constraining the atmospheric composition with transmission spectroscopy. *Astrophys J* 753, doi:10.1088/0004-637X/753/2/100.

Bétrémieux, Y. and Kaltenegger, L. (2014) Impact of atmospheric refraction: how deeply can we probe exo-Earth's atmospheres during primary eclipse observations? *Astrophys J* 791, doi:10.1088/0004-637X/791/1/7.

Botet, R., Rannou, P., and Cabane, M. (1997) Mean-field approximation of Mie scattering by fractal aggregates of identical spheres. *Appl Opt* 36:8791–8797.

Brasil, A.M., Farias, T.L., and Carvalho, M.G. (1999) A recipe for image characterization of fractal-like aggregates. *J Aerosol Sci* 30:1379–1389.

Byrne, B. and Goldblatt, C. (2015) Diminished greenhouse warming from Archean methane due to solar absorption lines. *Climate of the Past* 11:559–570.

Catling, D.C., Claire, M.W., Zahnle, K.J., Quinn, R.C., Clark, B.C., Hecht, M.H., and Kounaves, S. (2010) Atmospheric origins of perchlorate on Mars and in the Atacama. *J Geophys Res: Planets* 115, doi:10.1029/2009JE003425.

Chance, K. and Kurucz, R.L. (2010) An improved high-resolution solar reference spectrum for Earth's atmosphere measurements in the ultraviolet, visible, and near infrared. *J Quant Spectrosc Radiat Transf* 111:1289–1295.

Charnay, B., Forget, F., Wordsworth, R., Leconte, J., Millour, E., Codron, F., and Spiga, A. (2013) Exploring the faint young Sun problem and the possible climates of the Archean Earth with a 3-D GCM. *J Geophys Res: Atmospheres* 118:10414–10431.

Charnay, B., Meadows, V., Misra, A., Leconte, J., and Arney, G. (2015) 3D Modeling of GJ1214b's atmosphere: formation of inhomogeneous high clouds and observational implications. *Astrophys J* 813, doi:10.1088/2041-8205/813/1/L1.

Claire, M.W., Sheets, J., Cohen, M., Ribas, I., Meadows, V.S., and Catling, D.C. (2012) The evolution of solar flux from 0.1 nm to 160 $\mu$m: quantative estimates for planetary studies. *Astrophys J* 757, doi:10.1088/0004-637X/757/1/95.

Claire, M.W., Kasting, J.F., Domagal-Goldman, S.D., Stüeken, E.E., Buick, R., and Meadows, V.S. (2014) Modeling the signature of sulfur mass-independent fractionation produced in the Archean atmosphere. *Geochim Cosmochim Acta* 141:365–380.

Clark, R.N., Swayze, G.A., Wise, R., Livo, E., Kokaly, T., and Sutley, S.J. (2007) USGS digital spectral library splib06a. U.S. Geologial Survey, Digital Data Series 231. Available online at http://speclab.cr.usgs.gov/spectral.lib06

Clarke, D.W. and Ferris, J.P. (1997) Chemical evolution on Titan: comparisons to the prebiotic Earth. In *Planetary and Interstellar Processes Relevant to the Origins of Life*, edited by D.C.B. Whittett, Springer, Dordrecht, The Netherlands, pp 225–248.

Cockell, C.S. (1998) Biological effects of high ultraviolet radiation on early Earth—a theoretical evaluation. *J Theor Biol* 193:717–729.

Crisp, D. (1997) Absorption of sunlight by water vapor in cloudy conditions: a partial explanation for the cloud absorption anomaly. *Geophys Res Lett* 24:571–574.

Crow, C.A., McFadden, L.A., Robinson, T., Meadows, V.S., Livengood, T.A., Hewagama, T., Barry, R.K., Deming, L.D., Lisse, C.M., and Wellnitz, D. (2011) Views from EPOXI. Colors in our solar system as an analog for extrasolar planets. *Astrophys J* 729, doi:10.1088/0004-637X/729/2/130.

de Kok, R., Irwin, P.G.J., Teanby, N.A., Lellouch, E., Bézard, B., Vinatier, S., Nixon, C.A., Fletcher, L., Howett, C., Calcutt, S.B., Bowles, N.E., Flasar, F.M., and Taylor, F.W. (2007) Oxygen compounds in Titan's stratosphere as observed by Cassini CIRS. *Icarus* 186:354–363.

Denis, C., Schreider, A.A., Varga, P., and Závoti, J. (2002) Despinning of the Earth rotation in the geological past and geomagnetic paleointensities. *J Geodyn* 34:667–685.

DeWitt, H.L., Trainer, M.G., Pavlov, A.A., Hasenkopf, C.A., Aiken, A.C., Jimenez, J.L., McKay, C.P., Toon, O.B., and Tolbert, M.A. (2009) Reduction in haze formation rate on prebiotic Earth in the presence of hydrogen. *Astrobiology* 9:447–453.

Dillon, J.G. and Castenholz, R.W. (1999) Scytonemin, a cyanobacterial sheath pigment, protects against UVC radiation: implications for early photosynthetic life. *J Phycol* 35: 673–681.

Domagal-Goldman, S.D., Kasting, J.F., Johnston, D.T., and Farquhar, J. (2008) Organic haze, glaciations and multiple sulfur isotopes in the Mid-Archean Era. *Earth Planet Sci Lett* 269:29–40.

Domagal-Goldman, S.D., Meadows, V.S., Claire, M.W., and Kasting, J.F. (2011) Using biogenic sulfur gases as remotely detectable biosignatures on anoxic planets. *Astrobiology* 11:419–441.

Domagal-Goldman, S.D., Segura, A., Claire, M.W., Robinson, T.D., and Meadows, V.S. (2014) Abiotic ozone and oxygen in atmospheres similar to prebiotic Earth. *Astrophys J* 792, doi:10.1088/0004-637X/792/2/90.

Driese, S.G., Jirsa, M.A., Ren, M., Brantley, S.L., Sheldon, N.D., Parker, D., and Schmitz, M. (2011) Neoarchean paleoweathering of tonalite and metabasalt: implications for reconstructions of 2.69 Ga early terrestrial ecosystems and paleoatmospheric chemistry. *Precambrian Res* 189:1–17.

Eigenbrode, J.L. and Freeman, K.H. (2006) Late Archean rise of aerobic microbial ecosystems. *Proc Natl Acad Sci USA* 103:15759–15764.

Etiope, G. and Sherwood Lollar, B. (2013) Abiotic methane on Earth. *Rev Geophys* 51:276–299.

Farquhar, J., Huiming, B., and Thiemens, M. (2000) Atmospheric influence of Earth's earliest sulfur cycle. *Science* 289: 756–758.

Farquhar, J., Savarino, J., Airieau, S., and Thiemens, M.H. (2001) Observation of wavelength-sensitive mass-independent sulfur isotope effects during $SO_2$ photolysis: implications for the early atmosphere. *J Geophys Res* 106:32829–32839.

Farquhar, J., Peters, M., Johnston, D.T., Strauss, H., Masterson, A., Wiechert, U., and Kaufman, A.J. (2007) Isotopic evidence for Mesoarchaean anoxia and changing atmospheric sulphur chemistry. *Nature* 449:706–709.

García Muñoz, A., Zapatero Osorio, M.R., Barrena, R., Montañés-Rodríguez, P., Martín, E.L., and Pallé, E. (2012) Glancing views of the Earth: from a lunar eclipse to an exoplanetary transit. *Astrophys J* 755, doi:10.1088/0004-637X/755/2/103.

Goldblatt, C. and Zahnle, K.J. (2011) Clouds and the faint young Sun paradox. *Climate of the Past* 7:203–220.

Grenfell, J.L., Stracke, B., von Paris, P., Patzer, B., Titz, R., Segura, A., and Rauer, H. (2007) The response of atmospheric chemistry on Earthlike planets around F, G and K stars to small variations in orbital distance. *Planet Space Sci* 55:661–671.

Guzmán-Marmolejo, A., Segura, A., and Escobar-Briones, E. (2013) Abiotic production of methane in terrestrial planets. *Astrobiology* 13:550–559.

Hallquist, M., Wenger, J.C., Baltensperger, U., Rudich, Y., Simpson, D., Claeys, M., Dommen, J., Donahue, N.M., George, C., Goldstein, A.H., Hamilton, J.F., Herrmann, H., Hoffmann, T., Iinuma, Y., Jang, M., Jenkin, M.E., Jimenez, J.L., Kiendler-Scharr, A., Maenhaut, W., McFiggans, G., Mentel, Th.F., Monod, A., Prévôt, A.S.H., Seinfeld, J.H., Surratt, J.D., Szmigielski, R., and Wildt, J. (2009) The formation, properties and impact of secondary organic aerosol: current and emerging issues. *Atmos Chem Phys* 9:5155–5236.

Haqq-Misra, J.D., Domagal-Goldman, S.D., Kasting, P.J., and Kasting, J.F. (2008) A revised, hazy methane greenhouse for the Archean Earth. *Astrobiology* 8:1127–1137.

Harman, C.E., Kasting, J.F., and Wolf, E.T. (2013) Atmospheric production of glycolaldehyde under hazy prebiotic conditions. *Orig Life Evol Biosph* 43:77–98.

Harman, C.E., Schwieterman, E.W., Schottelkotte, J.C., and Kasting, J.F. (2015) Abiotic $O_2$ levels on planets around F, G, K, and M stars: possible false positives for life? *Astrophys J* 812, doi:10.1088/0004-637X/812/2/137.

Hasenkopf, C.A., Beaver, M.R., Trainer, M.G., Langley Dewitt, H., Freedman, M.A., Toon, O.B., McKay, C.P., and Tolbert, M.A. (2010) Optical properties of Titan and early Earth haze laboratory analogs in the mid-visible. *Icarus* 207:903–913.

Hasenkopf, C.A., Freedman, M.A., Beaver, M.R., Toon, O.B., and Tolbert, M.A. (2011) Potential climatic impact of organic haze on early Earth. *Astrobiology* 11:135–149.

Henyey, L.C. and Greenstein, J.L. (1941) Diffuse radiation in the Galaxy. *Astrophys J* 93:70–83.

Hicks, R.K., Day, D.A., Jimenez, J.L., and Tolbert, M.A. (2015) Elemental analysis of complex organic aerosol using isotopic labeling and unit-resolution mass spectrometry. *Anal Chem* 87:2741–2747.

Hörst, S.M. and Tolbert, M.A. (2013) *In situ* measurements of the size and density of Titan aerosol analogs. *Astrophys J* 770, doi:10.1088/2041-8205/770/1/L10.

Hörst, S.M., Yelle, R.V., Buch, A., Carrasco, N., Cernogora, G., Dutuit, O., Quirico, E., Sciamma-O'Brien, E., Smith, M.A., Somogyi, A., Szopa, C., Thissen, R., and Vuitton, V. (2012) Formation of amino acids and nucleotide bases in a Titan atmosphere simulation experiment. *Astrobiology* 12:809–817.

Imanaka, H., Cruikshank, D.P., Khare, B.N., and McKay, C.P. (2012) Optical constants of Titan tholins at mid-infrared wavelengths (2.5–25 $\mu$m) and the possible chemical nature of Titan's haze particles. *Icarus* 218:247–261.

Izon, G., Zerkle, A.L., Zhelezinskaia, I., Farquhar, J., Newton, R.J., Poulton, S.W., Eigenbrode, J.L., and Claire, M.W. (2015) Multiple oscillations in Neoarchaean atmospheric chemistry. *Earth Planet Sci Lett* 431:264–273.

Kaltenegger, L., Traub, W.A., and Jucks, K.W. (2007) Spectral evolution of an Earth-like planet. *Astrophys J* 658:598–616.

Kasting, J. and Ackerman, T. (1986) Climactic consequences of very high carbon dioxide levels in the Earth's early atmosphere. *Science* 234:1383–1385.

Kasting, J., Zahnle, K., Pinto, J., and Young, A. (1989) Sulfur, ultraviolet radiation, and the early evolution of life. *Orig Life Evol Biosph* 19:95–108.

Kasting, J.F. (1993) Earth's early atmosphere. *Science* 259:920–926.

Kasting, J.F. (2005) Methane and climate during the Precambrian era. *Precambrian Res* 137:119–129.

Kasting, J.F. and Donahue, T.M. (1980) The evolution of the atmospheric ozone. *J Geophys Res* 85:3255–3263.

Kasting, J.F., Liu, S.C., and Donahue, T.M. (1979) Oxygen levels in the prebiological atmosphere. *J Geophys Res* 84: 3097–3207.

Kelley, D.S., Karson, J.A., Fru, G.L., Yoerger, D.R., Shank, T.M., Butterfield, D.A., Hayes, J.M., Schrenk, M.O., Olson, E.J., Proskurowski, G., Jakuba, M., Bradley, A., Larson, B., Ludwig, K., Glickson, D., Buckman, K., Bradley, A.S., Brazelton, W.J., Roe, K., Elend, M.J., Delacour, A., Bernasconi, S.M., Lilley, M.D., Baross, J.A., Summons, R.E., and Sylva, S.P. (2005) A serpentinite-hosted ecosystem: the Lost City hydrothermal field. *Science* 307:1428–1434.

Khare, B.N., Sagan, C., Arakawa, E.T., Suits, F., Callcott, T.A., and Williams, M.W. (1984a) Optical constants of organic tholins produced in a simulated titanian atmosphere: from soft X-ray to microwave frequencies. *Icarus* 60:127–137.

Khare, B.N., Sagan, C., Thompson, W.R., Arakawa, E.T., Suits, F., Callcott, T.A., Williams, M.W., Shrader, S., Ogino, H., Willingham, T.O., and Nagy, B. (1984b) The organic aerosols of Titan. *Adv Space Res* 4:59–68.

Khare, B.N., Sagan, C., Ogino, H., Nagy, B., Er, C., Schram, K.H., and Arakawa, E.T. (1986) Amino acids derived from Titan tholins. *Icarus* 68:176–184.

Kharecha, P., Kasting, J., and Siefert, J. (2005) A coupled atmosphere-ecosystem model of the early Archean Earth. *Geobiology* 3:53–76.

Kitzmann, D., Patzer, A.B.C., von Paris, P., Godolt, M., Stracke, B., Gebauer, S., Grenfell, J.L., and Rauer, H. (2010) Clouds in the atmospheres of extrasolar planets I. Climatic effects of multi-layered clouds for Earth-like planets and implications for habitable zones. *Astron Astrophys* 511:1–14.

Kitzmann, D., Patzer, A.B.C., von Paris, P., Godolt, M., and Rauer, H. (2011a) Clouds in the atmospheres of extrasolar planets II. Thermal emission spectra of Earth-like planets influence by low and high-level clouds. *Astron Astrophys* 531:1–9.

Kitzmann, D., Patzer, A.B.C., von Paris, P., Godolt, M., and Rauer, H. (2011b) Clouds in the atmospheres of extrasolar planets III. Impact of low and high-level clouds on the reflection spectra of Earth-like planets. *Astron Astrophys* 531: A62.

Knutson, H., Benneke, B., Deming, D., and Homeier, D. (2014) A featureless transmission spectrum for the Neptune-mass exoplanet GJ 436b. *Nature* 505:66–68.

Kopparapu, R.K., Ramirez, R., Kasting, J.F., Eymet, V., Robinson, T.D., Mahadevan, S., Terrien, R.C., Domagal-Goldman, S., Meadows, V., and Deshpande, R. (2013) Habitable zones around main-sequence stars: new estimates. *Astrophys J* 765, doi10.1088/0004-637X/765/2/131.

Köylü, Ü.Ö., Faeth, G.M., Farias, T.L., and Carvalho, M.G. (1995) Fractal and projected structure properties of soot aggregates. *Combust Flame* 100:621–633.

Kreidberg, L., Bean, J.L., Désert, J.-M., Benneke, B., Deming, D., Stevenson, K.B., Seager, S., Berta-Thompson, Z., Seifahrt, A., and Homeier, D. (2014) Clouds in the atmosphere of the super-Earth exoplanet GJ 1214b. *Nature* 505:69–72.

Krissansen-Totton, J., Schwieterman, E.W., Charnay, B., Arney, G., Robinson, T.D., Meadows, V., and Catling, D.C. (2016) Is the Pale Blue Dot unique? Optimized photometric bands for identifying Earth-like exoplanets. *Astrophys J* 817, doi:10.3847/0004-637X/817/1/31.

Kunze, M., Godolt, M., Langematz, U., Grenfell, J.L., Hamann-Reinus, A., and Rauer, H. (2014) Investigating the early Earth faint young Sun problem with a general circulation model. *Planet Space Sci* 98:77–92.

Kurzweil, F., Claire, M., Thomazo, C., Peters, M., Hannington, M., and Strauss, H. (2013) Atmospheric sulfur rearrangement 2.7 billion years ago: evidence for oxygenic photosynthesis. *Earth Planet Sci Lett* 366:17–26.

Larson, E.J.L., Toon, O.B., West, R.A., and Friedson, A.J. (2015) Microphysical modeling of Titan's detached haze layer in a 3D GCM. *Icarus* 254:122–134.

Littler, M.M., Littler, D.S., Blair, S.M., and Norris, J.N. (1986) Deep-water plant communities from an uncharted seamount off San Salvador Island, Bahamas: distribution, abundance, and primary productivity. *Deep Sea Res A* 33:881–892.

López-Puertas, M., Dinelli, B.M., Adriani, A., Funke, B., García-Comas, M., Moriconi, M.L., D'Aversa, E., Boersma, C., and Allamandola, L.J. (2013) Large abundances of polycyclic aromatic hydrocarbons in Titan's upper atmosphere. *Astrophys J* 770, doi:10.1088/0004-637X/770/2/132.

Mahjoub, A., Carrasco, N., Dahoo, P.-R., Gautier, T., Szopa, C., and Cernogora, G. (2012) Influence of methane concentration on the optical indices of Titan's aerosols analogues. *Icarus* 221:670–677.

Manabe, S. and Wetherald, R.T. (1967) Thermal equilibrium of the atmosphere with a given distribution of relative humidity. *Journal of the Atmospheric Sciences* 24:241–259.

Marty, B., Zimmermann, L., Pujol, M., Burgess, R., and Philippot, P. (2013) Nitrogen isotopic composition and density of the Archean atmosphere. *Science* 342:101–104.

McDonald, G.D., Thompson, W.R., Heinrich, M., Khare, B.N., and Sagan, C. (1994) Chemical investigation of Titan and Triton tholins. *Icarus* 108:137–145.

McLinden, C.A., McConnell, J.C., Griffoen, E., McElroy, C.T., and Pfister, L. (1997) Estimating the wavelength-dependent ocean albedo under clear-sky conditions using NASA ER 2 spectroradiometer measurements. *J Geophys Res* 102:18801–18811.

Meadows, V. and Crisp, D. (1996) Ground-based near-infrared observations of the Venus nightside? The thermal structure and water abundance near the surface. *J Geophys Res: Planets* 101:4595–4622.

Meadows, V.S. (2006) Modelling the diversity of extrasolar terrestrial planets. *Proceedings of the International Astronomical Union* 1:25–34.

Misra, A., Meadows, V., Claire, M., and Crisp, D. (2014a) Using dimers to measure biosignatures and atmospheric pressure for terrestrial exoplanets. *Astrobiology* 14:67–86.

Misra, A., Meadows, V., and Crisp, D. (2014b) The effects of refraction on transit transmission spectroscopy: application to Earth-like exoplanets. *Astrophys J* 792, doi:10.1088/0004-637X/792/1/61.

Noffke, N. and Awramik, S.M. (2013) Stromatolites and MISS—differences between relatives. *GSA Today* 23:4–9.

Ono, S., Eigenbrode, J.L., Pavlov, A.A., Kharecha, P., Rumble, D., Kasting, J.F., and Freeman, K.H. (2003) New insights into Archean sulfur cycle from mass-independent sulfur isotope records from the Hamersley Basin, Australia. *Earth Planet Sci Lett* 213:15–30.

Pavlov, A. and Kasting, J. (2002) Mass-independent fractionation of sulfur isotopes in Archean sediments: strong evidence for an anoxic Archean atmosphere. *Astrobiology* 2:27–41.

Pavlov, A., Kasting, F., Brown, L.L., Rages, K.A., and Freedman, R. (2000) Greenhouse warming by $CH_4$ in the atmosphere of early Earth. *J Geophys Res* 105:11981–11990.

Pavlov, A., Kasting, J., Eigenbrode, J., and Freeman, K. (2001a) Organic haze in Earth's early atmosphere: source of low-$^{13}C$ Late Archean kerogens? *Geology* 29:1003–1006.

Pavlov, A., Brown, L., and Kasting, J. (2001b) UV shielding of $NH_3$ and $O_2$ by organic hazes in the Archean atmosphere. *J Geophys Res* 106:23267–23287.

Pierson, B., Mitchell, H., and Ruff-Roberts, A. (1992) *Chloroflexus aurantiacus* and ultraviolet radiation: implications for Archean shallow-water stromatolites. *Orig Life Evol Biosph* 23:243–260.

Planavsky, N.J., Reinhard, C.T., Wang, X., Thomson, D., McGoldrick, P., Rainbird, R.H., Johnson, T., Fischer, W.W., and Lyons, T.W. (2014) Low Mid-Proterozoic atmospheric oxygen levels and the delayed rise of animals. *Science* 346: 635–638.

Ramirez, R.M., Kopparapu, R., Zugger, M.E., Robinson, T.D., Freedman, R., and Kasting, J.F. (2013) Warming early Mars with $CO_2$ and $H_2$. *Nat Geosci* 7:59–63.

Ramirez, S., Coll, P., da Silva, A., Navarro-González, R., Lafait, J., and Raulin, F. (2002) Complex refractive index of Titan's aerosol analogues in the 200–900 nm domain. *Icarus* 156:515–529.

Rannou, P., Cabane, M., Botet, R., and Chassèfiere, E. (1997) A new interpretation of scattered light measurements at Titan's limb. *J Geophys Res* 102:10997–11013.

Robinson, T.D., Meadows, V.S., Crisp, D., Deming, D., A'hearn, M.F., Charbonneau, D., Livengood, T.A., Seager, S., Barry, R.K., Hearty, T., Hewagama, T., Lisse, C.M., McFadden, L.A., and Wellnitz, D.D. (2011) Earth as an extrasolar planet: Earth model validation using EPOXI earth observations. *Astrobiology* 11:393–408.

Robinson, T.D., Ennico, K., Meadows, V.S., Sparks, W., Bussey, D.B.J., Schwieterman, E.W., and Breiner, J. (2014a) Detection of ocean glint and ozone absorption using LCROSS Earth observations. *Astrophys J* 787, doi:10.1088/0004-637X/787/2/171.

Robinson, T.D., Maltagliati, L., Marley, M.S., and Fortney, J.J. (2014b) Titan solar occultation observations reveal transit spectra of a hazy world. *Proc Natl Acad Sci USA* 111:9042–9047.

Rothman, L.S., Gordon, I.E., Babikov, Y., Barbe, A., Chris Benner, D., Bernath, P.F., Birk, M., Bizzocchi, L., Boudon, V., Brown, L.R., Campargue, A., Chance, K., Cohen, E.A., Coudert, L.H., Devi, V.M., Drouin, B.J., Fayt, A., Flaud, J.-M., Gamache, R.R., Harrison, J.J., Hartmann, J.-M., Hill, C., Hodges, J.T., Jacquemart, D., Jolly, A., Lamouroux, J., LeRoy, R.J., Li, G., Long, D.A., Lyulin, O.M., Mackie, C.J., Massie, S.T., Mikhailenko, S., Müller, H.S.P., Naumenko, O.V., Nikitin, A.V., Orphal, J., Perevalov, V., Perrin, A., Polovtseva, E.R., Richard, C., Smith, M.A.H., Starikova, E., Sung, K., Tashkun, S., Tennyson, J., Toon, G.C., Tyuterev, Vl.G., and Wagner, G. (2013) The HITRAN2012 molecular spectroscopic database. *J Quant Spectrosc Radiat Transf* 130:4–50.

Rugheimer, S., Kaltenegger, L., Zsom, A., Segura, A., and Sasselov, D. (2013) Spectral fingerprints of Earth-like planets around FGK stars. *Astrobiology* 13:251–269.

Rugheimer, S., Segura, A., Kaltenegger, L., and Sasselov, D. (2015) UV surface environment of Earth-like planets orbiting FGKM stars through geological evolution. *Astrophys J* 806, doi:10.1088/0004-637X/806/1/137.

Sagan, C. and Chyba, C. (1997) The early faint young Sun paradox: organic shielding of ultraviolet-labile greenhouse gases. *Science* 276:1217–1221.

Sagan, C., Thompson, W.R., Carlson, R., Gurnett, D., and Hord, C. (1993) A search for life on Earth from the Galileo spacecraft. *Nature* 365:715–721.

Schidlowski, M. (2001) Carbon isotopes as biogeochemical recorders of life over 3.8 Ga of Earth history: evolution of a concept. *Precambrian Res* 106:117–134.

Schopf, J.W., editor. (1983) *Earth's Earliest Biosphere: Its Origin and Evolution*, Princeton University Press, Princeton, NJ.

Schwieterman, E.W., Meadows, V.S., Domagal-Goldman, S.D., Deming, D., Arney, G.N., Luger, R., Harman, C.E., Misra, A., and Barnes, R. (2016) Identifying planetary biosignature impostors: spectral features of CO and $O_4$ resulting from abiotic $O_2/O_3$ production. *Astrophys J* 819, doi:10.3847/2041-8205/819/1/L13.

Sciamma-O'Brien, E., Dahoo, P.-R., Hadamcik, E., Carrasco, N., Quirico, E., Szopa, C., and Cernogora, G. (2012) Optical constants from 370nm to 900nm of Titan tholins produced in a low pressure RF plasma discharge. *Icarus* 218:353–363.

Sebree, J.A., Stern, J.C., Mandt, K.E., Domagal-Goldman, S.D., and Trainer, M.G. (2015) C and $^{15}N$ fractionation of $CH_4/N_2$ mixtures during photochemical aerosol formation: relevance to Titan. *Icarus* 2:1–8.

Segura, A., Krelove, K., Kasting, J.F., Sommerlatt, D., Meadows, V., Crisp, D., Cohen, M., and Mlawer, E. (2003) Ozone concentrations and ultraviolet fluxes on Earth-like planets around other stars. *Astrobiology* 3:689–708.

Segura, A., Kasting, J.F., Meadows, V., Cohen, M., Scalo, J., Crisp, D., Butler, R.A.H., and Tinetti, G. (2005) Biosignatures from Earth-like planets around M dwarfs. *Astrobiology* 5:706–725.

Segura, A., Meadows, V., Kasting, J., Crisp, D., and Cohen, M. (2007) Abiotic formation of $O_2$ and $O_3$ in high-$CO_2$ terrestrial atmospheres. *Astron Astrophys* 472:665–679.

Segura, A., Walkowicz, L.M., Meadows, V., Kasting, J., and Hawley, S. (2010) The effect of a strong stellar flare on the atmospheric chemistry of an Earth-like planet orbiting an M dwarf. *Astrobiology* 10:751–771.

Shaw, G.H. (2008) Earth's atmosphere—Hadean to early Proterozoic. *Chemie der Erde - Geochemistry* 68:235–264.

Shields, A.L., Meadows, V.S., Bitz, C.M., Pierrehumbert, R.T., Joshi, M.M., and Robinson, T.D. (2013) The effect of host star spectral energy distribution and ice-albedo feedback on the climate of extrasolar planets. *Astrobiology* 13:715–739.

Sing, D.K., Pont, F., Aigrain, S., Charbonneau, D., Désert, J.-M., Gibson, N., Gilliland, R., Hayek, W., Henry, G., Knutson, H., Lecavelier des Etangs, A., Mazeh, T., and Shporer, A. (2011) Hubble Space Telescope transmission spectroscopy of the exoplanet HD 189733b: high-altitude atmospheric haze in the optical and near-ultraviolet with STIS. *Mon Not R Astron Soc* 416:1443–1455.

Som, S.M., Catling, D.C., Harnmeijer, J.P., Polivka, P.M., and Buick, R. (2012) Air density 2.7 billion years ago limited to less than twice modern levels by fossil raindrop imprints. *Nature* 484:359–362.

Thomassot, E., O'Neil, J., Francis, D., Cartigny, P., and Wing, B.A. (2015) Atmospheric record in the Hadean eon from multiple sulfur isotope measurements in Nuvvuagittuq greenstone belt (Nunavik, Quebec). *Proc Natl Acad Sci USA* 112:707–712.

Thomazo, C., Ader, M., Farquhar, J., and Philippot, P. (2009) Methanotrophs regulated atmospheric sulfur isotope anomalies during the Mesoarchean (Tumbiana Formation, Western Australia). *Earth Planet Sci Lett* 279:65–75.

Tolfo, F. (1977) A simplified model of aerosol coagulation. *J Aerosol Sci* 8:9–19.

Tomasko, M.G., Doose, L., Engel, S., Dafoe, L., West, R., Lemmon, M., Karkoschfka, E., and See, C. (2008) A model of Titan's aerosols based on measurements made inside the atmosphere. *Planet Space Sci* 56:669–707.

Toon, O.B., Mckay, C.P., Ackerman, T.P., and Santhanam, K. (1989) Rapid calculation of radiative heating rates and photodissociation rates in inhomogeneous multiple scattering atmospheres. *J Geophys Res* 94:16287–16301.

Trainer, M.G. (2013) Atmospheric prebiotic chemistry and organic hazes. *Current Organic Chemistry* 17:1710–1723.

Trainer, M.G., Pavlov, A.A., Curtis, D.B., McKay, C.P., Worsnop, D.R., Delia, A.E., Toohey, D.W., Toon, O.B., and Tolbert, M.A. (2004) Haze aerosols in the atmosphere of early Earth: manna from heaven. *Astrobiology* 4:409–419.

Trainer, M.G., Pavlov, A.A., DeWitt, H.L., Jimenez, J.L., McKay, C.P., Toon, O.B., and Tolbert, M.A. (2006) Organic haze on Titan and the early Earth. *Proc Natl Acad Sci USA* 103:18035–18042.

Trainer, M.G., Jimenez, J.L., Yung, Y.L., Toon, O.B., and Tolbert, M.A. (2012) Nitrogen incorporation in $CH_4$-$N_2$ photochemical aerosol produced by far ultraviolet irradiation. *Astrobiology* 12:315–326.

Tran, B.N., Joseph, J.C., Ferris, J.P., Persans, P.D., and Chera, J.J. (2003) Simulation of Titan haze formation using a photochemical flow reactor. The optical constant of the polymer. *Icarus* 165:379–390.

Traub, W.A. (2003) Extrasolar planet characteristics in the visible wavelength range. In *Proceedings of the Conference on Towards Other Earths: DARWIN/TPF and the Search for Extrasolar Terrestrial Planets*, Heidelberg, Germany, pp 231–239.

Ueno, Y., Yamada, K., Yoshida, N., Maruyama, S., and Isozaki, Y. (2006) Evidence from fluid inclusions for microbial methanogenesis in the early Archaean era. *Nature* 440:516–519.

Urey, H.C. and Greiff, L.J. (1935) Isotopic exchange equilibria. *J Am Chem Soc* 57:321–327.

Vuitton, V., Tran, B.N., Persans, P.D., and Ferris, J.P. (2009) Determination of the complex refractive indices of Titan haze analogs using photothermal deflection spectroscopy. *Icarus* 203:663–671.

Waite, J.H., Young, D.T., Cravens, T.E., Coates, A.J., Crary, F.J., Magee, B., and Westlake, J. (2007) The process of tholin formation in Titan's upper atmosphere. *Science* 316:870–875.

Watanabe, Y., Martini, J.E.J., and Ohmoto, H. (2000) Geochemical evidence for terrestrial ecosystems 2.6 billion years ago. *Nature* 408:574–578.

Woese, C.R. and Fox, G.E. (1977) Phylogenetic structure of the prokaryotic domain: the primary kingdoms. *Proc Natl Acad Sci USA* 74:5088–5090.

Wolf, E.T. and Toon, O.B. (2010) Fractal organic hazes provided an ultraviolet shield for early Earth. *Science* 328:1266–1268.

Wolf, E.T. and Toon, O.B. (2013) Hospitable Archean climates simulated by a general circulation model. *Astrobiology* 13:656–673.

Woolf, N.J., Smith, P.S., Traub, W.A., and Jucks, K.W. (2002) The spectrum of Earthshine: a pale blue dot observed from the ground. *Astrophys J* 574:430–433.

Workman, J., editor. (2000) *The Handbook of Organic Compounds, Three-Volume Set: NIR, IR, R, and UV-Vis Spectra Featuring Polymers and Surfactants*, Academic Press, San Diego, CA.

Wright, G.S., Rieke, G.H., Colina, L., van Dishoeck, E., Goodson, G., Greene, T., Lagage, P.-O., Karnik, A., Lambros, S.D., Lemke, D., Meixner, M., Norgaard, H.-U., Oloffson, G., Ray, T., Ressler, M., Waelkens, C., Wright, D., and Zhender, A. (2004) The JWST MIRI instrument concept. *Proc SPIE* 5487:653–663.

Yoon, Y.H., Hörst, S.M., Hicks, R.K., Li, R., de Gouw, J.A., and Tolbert, M.A. (2014) The role of benzene photolysis in Titan haze formation. *Icarus* 233:233–241.

Young, G.M., von Brunn, V., Gold, D.J.C., and Minter, W.E.L. (1998) Earth's oldest reported glaciation: physical and chemical evidence from the Archean Mozaan Group (~2.9 Ga) of South Africa. *J Geol* 106:523–538.

Yung, Y.L., Allen, M., and Pinto, J.P. (1984) Photochemistry of the atmosphere of Titan: comparison between model and observations. *Astrophys J Suppl Ser* 55:465–506.

Zahnle, K., Claire, M., and Catling, D. (2006) The loss of mass-independent fractionation in sulfur due to a Palaeoproterozoic collapse of atmospheric methane. *Geobiology* 4:271–283.

Zerkle, A.L., Claire, M.W., Domagal-Goldman, S.D., Farquhar, J., and Poulton, S.W. (2012) A bistable organic-rich atmosphere on the Neoarchaean Earth. *Nat Geosci* 5:359–363.

Address correspondence to:
*Giada Arney*
*NASA/GSFC*
*Mail Code: 699*
*Greenbelt, MD 20771*

*E-mail:* giada.n.arney@nasa.gov

Submitted 20 October 2015
Accepted 13 July 2016

## Abbreviations List

CAM = Community Atmosphere Model
GCM = General Circulation Model
GOE = Great Oxygenation Event
LMD = Laboratoire de Météorologie Dynamique
MDF = mass-dependent fractionation
MIF = mass-independent fractionation
NIR = near infrared
PAL = present atmospheric level
SMART = Spectral Mapping Atmospheric Radiative Transfer
SZA = solar zenith angle